Hindawi
Advances in Civil Engineering
Volume 2021, Article ID 8867536, 33 pages
https://doi.org/10.1155/2021/8867536

Research Article

Analytical Solutions for the Mechanical Responses of Shallow Double-Arched Tunnel Subjected to Symmetric Loads

Song Yang,[1,2] **Rui Dai**,[3] **Zubin Ai**,[2] **Xiaochang Li**,[4] **Chao Zhang**,[2] **and Xin Huang**[4]

[1]*School of Civil Engineering, Tsinghua University, Beijing 100048, China*
[2]*POWERCHINA Roadbridge Group Co., Ltd, Beijing 100048, China*
[3]*Bureau of Transporation, Honghe Hani and Yi Autonomous Prefecture, Yunnan Province 661400, China*
[4]*Department of Geotechnical Engineering, College of Civil Engineering, Tongji University, Shanghai 200092, China*

Correspondence should be addressed to Xiaochang Li; lixiaochang@tongji.edu.cn

Received 10 June 2020; Revised 27 December 2020; Accepted 30 January 2021; Published 26 April 2021

Academic Editor: Marco Corradi

Copyright © 2021 Song Yang et al. This is an open access article distributed under the Creative Commons Attribution License, which permits unrestricted use, distribution, and reproduction in any medium, provided the original work is properly cited.

Double-arched tunnel is a special kind of tunnel structure which is widely adopted for shallow rock tunnels. The internal forces within a double-arched tunnel are difficult to be determined due to its special geometry and complex interactions with surrounding rock masses. This paper presents a set of analytical solutions for determining the internal forces within the lining structure of shallow double-arched tunnel subjected to symmetric external loads. The double-arched tunnel is decomposed into three main parts, i.e., the arch rings, the side walls, and the middle wall. The force method and the elastic foundation beam model are employed for the arch rings and the side walls, respectively, while the middle wall is treated as a cantilever beam fixed at the bottom. Analytical solutions for the internal forces of the three parts are derived separately, which are continuous at the conjunctions of different parts. The derived analytical solutions are verified by comparing with the FEM simulation results. Finally, parametric studies are performed to investigate the influences of burial depth, elastic resistance coefficient, opening angle, and tunnel span on the internal forces based on which some recommendations are provided for the construction and design of the double-arched tunnels. The derived analytical solutions provide fast estimations for the internal forces and deformation of the double-arched lining structures, which will be a useful tool for design optimization.

1. Introduction

The double-arched tunnel is a special kind of tunnel whose lining structures between two adjacent tunnels are connected and supported by the middle wall [1].

Unlike single tunnels with a circular or straight wall arch cross section which have been profoundly investigated [2–9], due to its special geometry, the distribution of internal forces of double-arched tunnels has not yet been well understood. Yan et al. set up a comprehensive monitoring program at critical sections of a double-arched tunnel to measure the internal forces in both steel arches and secondary linings [10]. The monitoring and analysis results show that the forces of lining structures are directly related to multiple factors, including the construction procedures, geological conditions, and locations in the double-arched tunnel. They further showed that the arch vault is the most critical section, which was also observed by Yuan et al. [11]. Through in-site monitoring, Lai et al. found that the critical areas of double-arched tunnels are mainly located on the middle wall, side wall, and vault [12]. Zhang et al. carried out a model test for an unequally spanned double-arched tunnel to study the distribution of surrounding rock pressure and mechanical characteristics and found that the tunnel was in a small eccentric bending state, and thrust stress in the side walls increases with increasing span [13]. He et al. conducted model tests to investigate the distribution of internal forces of nonsymmetric double-arched tunnels in sand-cobble ground [14]. They showed that the internal force of the structure increased linearly with the increase in external load until the first crack appeared, after which the internal force redistributed but the structure still had a certain bearing

capacity. Li et al. derived the mechanical responses of supporting structure for a shallow-buried double-arched tunnel under the China Great Wall based on reduced-scale model tests [15].

Numerical simulations have also been conducted to analyse the stability and mechanical behaviours of double-arched lining structure. Yu and Yang analysed the internal force of the lining of the double-arched tunnel by using the loading structure method, considering the situations of both single-side and double-side bearings [16]. Zhang and He performed numerical simulations on the mechanical behaviour of middle wall of double-arched tunnel and found that the main factors affecting the loads of middle wall include the burial depth, the properties of surrounding rock, the construction method, and the eccentric loading condition [17]. Based on the coupled fluid-solid theorem, Li et al. investigated the stability of surrounding rock and internal forces of double-arched tunnel under seepage condition [18]. Mao et al. simulated the construction process of a double-arched tunnel in loess area considering the lateral recharge and fluid-solid coupling effect, which showed that the water disaster susceptible areas mainly are concentrated in the middle wall, arch springs of both tunnels, and tunnel face [19]. Liu et al. studied the acceleration response of a shallow-buried biased double-arched tunnel under the action of Wenchuan wave [20]. Based on both physical model testing and numerical simulation results, Min et al. reported that the presence of voids on the top of the middle wall may induce adverse effects on the lining, which are characterized by significant change of internal forces and increase in lining deformation [21]. Similarly, Zhang et al. showed that the internal forces change significantly at the area in the close vicinity of the void [22].

The aforementioned studies are either costly or time-consuming. In contrast, analytical approach is a convenient, fast, and effective method for analysing the mechanical behaviour of both surrounding ground and tunnel lining [23–25]. Based on Airy's stress function, Nagger and Hinchberger presented a closed-form solution for bending moment and thrust force of tunnel linings that can be idealized as an inner jointed segmental lining and an outer thick-walled cylinder embedded in a homogeneous infinite elastic soil or rock, accounting for the interaction between the lining and the surrounding ground [26]. Lee et al. adopted the force method to predict internal forces and displacements of a jointed circular segmental tunnel lining by treating the longitudinal joints as a set of linear rotational springs [27]. Wang et al. presented an analytical solution for circular segmental tunnel lining based on the state space method [28]. The curved Euler beam theory and the principle of minimum potential energy were adopted during the derivation of governing equations. Wang et al. further derived a unified analytical solution for the circular segmental tunnel lining irrespective of the layout of segmental assemblies between adjacent rings by modelling the interaction between the segments as a set of springs with three-directional resistances [29]. Talmon and Bezuijen presented an analytical model to analyse the longitudinal bending moment in the tunnel lining during the construction phase of bored tunnels, taking into account the influence of forces from the TBM, the loading of the tunnel lining by the grout in the liquid phase, and linear elastic properties of the tunnel lining and soil [30]. Zhao et al. employed the commonly accepted analytical solutions to calculate the lining forces and deformations for both shallow and deep tunnels [31]. Park et al. developed an analytical solution by considering the relationships between displacements and interaction forces at the soil-lining interface and including the slippage effect at the soil-lining interface using a spring-type flexibility coefficient [32]. Bobet presented closed-form solutions for the liner stresses of a deep circular tunnel excavated in transversely anisotropic rock [33]. Kargar et al. provided a semianalytical elastic plane-strain solution for stress field around a lined noncircular tunnel at great depth subjected to uniform ground load [34]. The analytical solution for an arbitrarily shaped tunnel excavated in anisotropic rock mass supported by an isotropic lining was presented by Wang et al. [35]. The equations and solutions of stresses and displacements in lining and surrounding rock mass were derived based on the complex variable method.

Most of the research studies about analytical approach mentioned above mainly focus on the internal forces or stresses of single tunnel lining, especially for the circular tunnel due to the simplification and convenience in the derivation. Hu et al. presented an analytical solution for the determination of internal forces of a jointed segmental precast DOT (double-O-tube) lining by combining the unbalanced force transition method with the force method [23]. This is the only analytical work available for the double tunnel lining. However, it should be noted that the shape of the DOT lining is still relatively regular when comparing with the double-arched tunnel which is normally composed of arch rings, straight side walls, and middle wall. So far, no analytical solutions for the internal forces of double-arched tunnel have been reported in the literature.

In this paper, analytical solutions for determining the internal forces of lining structure in shallow double-arched tunnels subjected to symmetric loading are presented. The double-arched tunnel is decomposed into three parts, including the arch rings, the side walls, and the middle walls. The force method is applied to determine the internal forces of arch rings. The elastic foundation beam model is employed for representing the side walls. The middle wall is treated as a cantilever beam fixed at the bottom. The internal forces are continuous at the conjunctions of the three different parts. The internal forces of a background project calculated using the proposed analytical solutions are compared with the values obtained by the numerical simulations. Finally, based on the obtained analytical solutions, parametric analyses are conducted to investigate the influences of some key influential factors on the internal forces of the double-arched tunnel lining.

2. Model Formulation

During the derivation, the following basic assumptions and methodologies are adopted:

(1) The double-arched tunnel is shallowly buried
(2) The middle wall of the double-arched tunnel is straight and can be taken as a cantilever beam while the side wall is assumed as an elastic foundation beam
(3) The bottom of the side wall is fixed in both horizontal and vertical directions but can rotate under the elastic resistance, while the bottom of the middle wall is fixed
(4) The inverted arch is not considered in the derivation of the analytical solution
(5) The analytical solutions for the internal forces along the tunnel arch, the middle wall, and the side walls are derived separately
(6) The force method and elastic foundation beam method are used for the derivation of internal forces along the tunnel arch and side wall, respectively
(7) The thicknesses of the tunnel lining and the middle wall are not considered during the derivation and the external dimensions of the lining are employed
(8) The tunnel lining is considered as linear elastic

Based on the above assumptions, the original mechanical model presented in Figure 1(a) could be simplified into Figure 1(b). The definitions of symbols presented in Figure 1 are given as follows: H is the burial depth at the crown of the double-arched tunnel; H_1 is the height from the top of the middle wall to the ground surface; H_2 is the height of the double-arched tunnel; B is the total width of the double-arched tunnel; R is the outer radius of the arch ring of left tunnel; α_1, α_2, and α_3 can be considered as the growth angle of lateral earth pressure along depth of the corresponding three kind of pressures, which are given by $\tan\alpha_1 = (e_2 - e_1)/H_2$ and $\tan\alpha_2 = (e_2' - e_1')/f_2$, $\alpha_3 = q'/l_2$; a denotes the bottom point of the side wall in the left tunnel; h is the foot of left arch of left tunnel on the top of the side wall; d is the foot of right arch of left tunnel on the top of middle wall; l is the height of the side wall of left tunnel; l_1 and l_2 are the widths of left and right half arch rings of left tunnel, respectively; f_1 and f_2 are the height of left and right half arch rings of left tunnel; and h_a denotes the bottom width of the left side wall. A prime is added to the same set of symbols to denote the corresponding quantities of the right tunnel. The external pressure from the surrounding rock mass is determined under the assumption that the double-arched tunnel is shallowly buried [36, 37].

The cut-off altitude (H_p) separating deep tunnel from shallow tunnel can be considered as follows:

$$H_p = (2 \sim 2.5)h_p, \tag{1}$$

where h_p is the load equivalent height, which can be calculated according to the approach proposed by [36, 37].

As shown in Figure 1(a), based on H_p and h_p, the pressure of shallow double-arched tunnel can be determined according to two different conditions as shown in Table 1 [36].

In Table 1, γ is the unit weight of the surrounding rock mass, φ is the calculated friction angle of surrounding rock masses, λ is the lateral pressure coefficient, β is the angle between the failure surfaces and the horizontal for both sides of the tunnel, and θ is the friction angle of sliding surface, which can be determined according to Table 2.

3. Model Derivation

In this section, the analytical solutions for the internal forces of arch ring, side wall, and middle wall are derived separately based on the simplified model given in Figure 1(b). Since the structure configuration and pressure distribution are both symmetric, only the left part of the tunnel structure is employed in the following derivation. The internal forces of the middle wall can be obtained by the superposition of corresponding quantities from both arch rings.

3.1. Analytical Solutions for the Arch Rings. The simplified models of the left arch ring for the force method are presented in Figure 2. All the pressures exerted on the arch rings shown in Figure 2 are considered as active pressures, which are all positive. The redundant internal forces of the crown section of the arch ring induced by the active pressures are X_{1p}, X_{2p}, and X_{3p}, respectively. The angular displacement of the arch foot turning outwards, the outward horizontal displacement, the upward vertical displacement of the right arch foot, and the downward vertical displacement of the left arch foot are positive.

β_{pl}, u_{pl}, and v_{pl} represent the angular, horizontal, and vertical displacements of the left arch foot, respectively, while β_{pr}, u_{pr}, and v_{pr} denote the same quantities of the right arch foot.

According to the displacement coordination condition of the force method at the crown of the arch ring, the displacement equations are as follows:

$$\left.\begin{aligned}
&X_{1p}\delta_{11} + X_{2p}\delta_{12} + X_{3p}\delta_{13} + \Delta_{1p} + \beta_{\mathrm{pl}} + \beta_{\mathrm{pr}} = 0\\
&X_{1p}\delta_{21} + X_{2p}\delta_{22} + X_{3p}\delta_{23} + \Delta_{2p} + u_{\mathrm{pl}} + u_{\mathrm{pr}} + f_1\beta_{\mathrm{pl}} + f_2\beta_{\mathrm{pr}} = 0\\
&X_{1p}\delta_{31} + X_{2p}\delta_{32} + X_{3p}\delta_{33} + \Delta_{3p} + v_{\mathrm{pl}} + v_{\mathrm{pr}} + l_2\beta_{\mathrm{pr}} - l_1\beta_{\mathrm{pl}} = 0
\end{aligned}\right\}, \tag{2}$$

where $\delta_{ij} = (i, j = 1, 2, 3)$ are the flexibility coefficients of the arch ring and Δ_{ip} is the displacement induced by the active pressure in the direction of X_{ip} at the cross section of the tunnel crown.

By using the superposition principle, the displacements of the left and right arch feet are obtained as follows:

$$\left.\begin{aligned}
\beta_{\mathrm{pl}} &= X_{1p}\beta_{1l} + X_{2p}(\beta_{2l} + f_1\beta_{1l}) + X_{3p}(\beta_{3l} - l_1\beta_{1l}) + \beta_{\mathrm{pl}}^{o}\\
\beta_{\mathrm{pr}} &= X_{1p}\beta_{1r} + X_{2p}(\beta_{2r} + f_2\beta_{1r}) + X_{3p}(\beta_{3r} + l_2\beta_{1r}) + \beta_{\mathrm{pr}}^{o}\\
u_{\mathrm{pl}} &= X_{1p}u_{1l} + X_{2p}(u_{2l} + f_1u_{1l}) + X_{3p}(u_{3l} - l_1u_{1l}) + u_{\mathrm{pl}}^{o}\\
u_{\mathrm{pr}} &= X_{1p}u_{1r} + X_{2p}(u_{2r} + f_2u_{1r}) + X_{3p}(u_{3r} + l_2u_{1r}) + u_{\mathrm{pr}}^{o}\\
v_{\mathrm{pl}} &= X_{1p}v_{1l} + X_{2p}(v_{2l} + f_1v_{1l}) + X_{3p}(v_{3l} - l_1v_{1l}) + v_{\mathrm{pl}}^{o}\\
v_{\mathrm{pr}} &= X_{1p}v_{1r} + X_{2p}(v_{2r} + f_2v_{1r}) + X_{3p}(v_{3r} + l_2v_{1r}) + v_{\mathrm{pr}}^{o}
\end{aligned}\right\}, \tag{3}$$

where β_{il}, u_{il}, and v_{il} are the angular, horizontal, and vertical displacements of the left arch foot under the unit loads

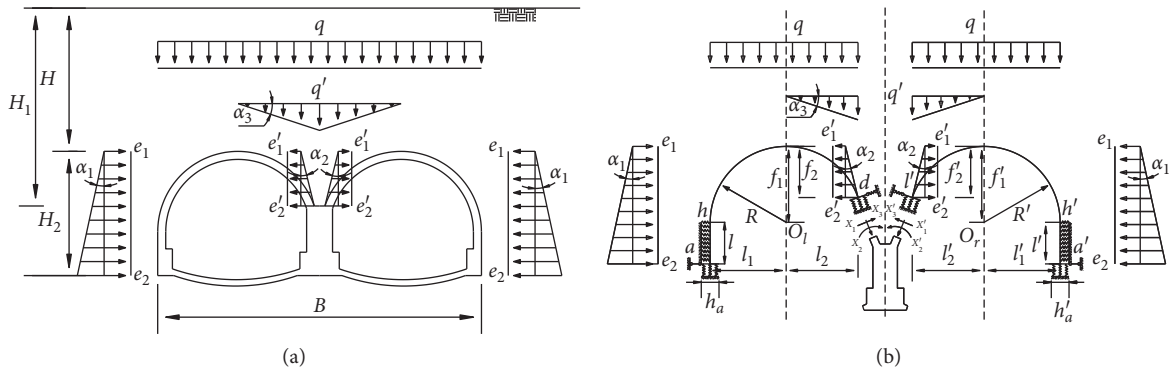

Figure 1: The model of double-arched tunnel: (a) the mechanical model; (b) the simplified mechanical model (explanations for each symbol are allied with the first place it appears in the paper).

Table 1: The pressures on the double-arched tunnel.

Scenario 1, $H \le h_p$	Scenario 2, $h_p < H \le H_p$	Notes
$q = \gamma H$ $e_1 = \gamma H \tan^2(45^\circ - (\varphi/2))$ $e_2 = \gamma(H + H_2)\tan^2(45^\circ - (\varphi/2))$ $q' = \gamma(H_1 - H)$ $e_1' = q \tan^2(45 - (\varphi/2))$ $e_2' = (q + q')\tan^2(45^\circ - (\varphi/2))$	$q = \gamma H(1 - (H/B)\lambda \tan\theta)$ $e_1 = \lambda\gamma H$ $e_2 = \lambda\gamma(H + H_2)$	$\lambda = (\tan\beta - \tan\varphi)/(\tan\beta[1 + \tan\beta(\tan\varphi - \tan\theta)\tan\varphi\tan\theta])$ $\tan\beta = \tan\phi + \sqrt{((\tan\varphi(\tan^2\varphi + 1))/(\tan\varphi - \tan\theta))}$ \

Table 2: The θ values for different grades of surrounding rock [38].

Surrounding rock grade	I, II, III	IV	V	VI
θ	0.9 φ	(0.7–0.9)φ	(0.5–0.7)φ	(0.3–0.5)φ

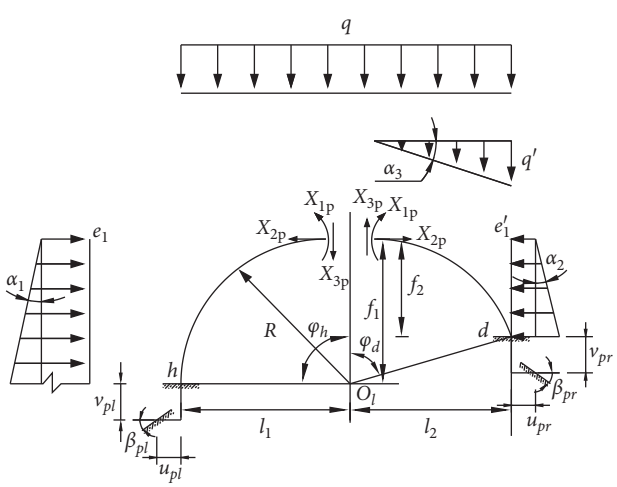

Figure 2: The simplified model for the left arch ring.

$X_i = 1\,(i = 1, 2, 3)$, respectively; β_{ir}, u_{ir}, and v_{ir} denote the same quantities of the right arch foot; β^o_{pl}, u^o_{pl}, and v^o_{pl} are the angular, horizontal, and vertical displacements of the left arch foot under the active pressures; and β^o_{pr}, u^o_{pr}, and v^o_{pr} are the same quantities of the right arch foot.

The reciprocal theorem of displacement gives the following relationships:

$$\begin{aligned} \beta_{2l} &= u_{1l}, \\ \beta_{3l} &= v_{1l}, \\ u_{3l} &= v_{2l}, \\ \beta_{2r} &= u_{1r}, \\ \beta_{3r} &= v_{1r}, \\ u_{3r} &= v_{2r}. \end{aligned} \tag{4}$$

Substituting the displacements in equation (3) into equation (2), the following displacement equations containing the unknown X_{1p}, X_{2p}, and X_{3p} are obtained:

$$\left.\begin{aligned} a_{11}X_{1p} + a_{12}X_{2p} + a_{13}X_{3p} + a_{10} &= 0 \\ a_{21}X_{1p} + a_{22}X_{2p} + a_{23}X_{3p} + a_{20} &= 0 \\ a_{31}X_{1p} + a_{32}X_{2p} + a_{33}X_{3p} + a_{30} &= 0 \end{aligned}\right\}, \tag{5}$$

where the coefficients a_{ij} are determined by the following:

$$\left.\begin{aligned}
a_{11} &= \delta_{11} + \beta_{1l} + \beta_{1r} \\
a_{12} &= \delta_{12} + \beta_{2l} + \beta_{2r} + f_1\beta_{1l} + f_2\beta_{1r} \\
a_{13} &= \delta_{13} + \beta_{3l} + \beta_{3r} + l_2\beta_{1r} - l_1\beta_{1l} \\
a_{10} &= \Delta_{1p} + \beta_{\mathrm{pl}}^{o} + \beta_{\mathrm{pr}}^{o} \\
a_{21} &= \delta_{21} + u_{1l} + u_{1r} + f_1\beta_{1l} + f_2\beta_{1r} \\
a_{22} &= \delta_{22} + u_{2l} + u_{2r} + f_1u_{1l} + f_2u_{1r} + f_1\beta_{2l} + f_1^2\beta_{1l} + f_2\beta_{2r} + f_2^2\beta_{1r} \\
a_{23} &= \delta_{23} + u_{3l} + u_{3r} + l_2u_{1r} - l_1u_{1l} + f_1\beta_{3l} - f_1l_1\beta_{1l} + f_2\beta_{3r} + f_2l_2\beta_{1r} \\
a_{20} &= \Delta_{2p} + u_{\mathrm{pl}}^{o} + u_{\mathrm{pr}}^{o} + f_1\beta_{\mathrm{pl}}^{o} + f_2\beta_{\mathrm{pr}}^{o} \\
a_{31} &= \delta_{31} + v_{1l} + v_{1r} + l_2\beta_{1r} - l_1\beta_{1l} \\
a_{32} &= \delta_{32} + v_{2l} + v_{2r} + f_1v_{1l} + f_2v_{1r} + l_2\beta_{2r} + l_2f_2\beta_{1r} - l_1\beta_{2l} - l_1f_1\beta_{1l} \\
a_{33} &= \delta_{33} + v_{3l} + v_{3r} - l_1v_{1l} + l_2v_{1r} + l_2\beta_{3r} + l_2^2\beta_{1r} - l_1\beta_{1l} + l_1^2\beta_{1l} \\
a_{30} &= \Delta_{3p} + v_{\mathrm{pl}}^{o} + v_{\mathrm{pr}}^{o} + l_2\beta_{\mathrm{pr}}^{o} - l_1\beta_{\mathrm{pl}}^{o}
\end{aligned}\right\}. \tag{6}$$

By solving equation (5), X_{1p}, X_{2p}, and X_{3p} can be determined as follows:

$$\left.\begin{aligned}
X_{1p} &= \frac{\Delta_1}{\Delta} \\
X_{2p} &= \frac{\Delta_2}{\Delta} \\
X_{3p} &= \frac{\Delta_3}{\Delta}
\end{aligned}\right\}, \tag{7}$$

where $\Delta = \begin{bmatrix} a_{11} & a_{12} & a_{13} \\ a_{21} & a_{22} & a_{23} \\ a_{31} & a_{32} & a_{33} \end{bmatrix}$, $\Delta_1 = -\begin{bmatrix} a_{10} & a_{12} & a_{13} \\ a_{20} & a_{22} & a_{23} \\ a_{30} & a_{32} & a_{33} \end{bmatrix}$, $\Delta_2 = -\begin{bmatrix} a_{11} & a_{10} & a_{13} \\ a_{21} & a_{20} & a_{23} \\ a_{31} & a_{30} & a_{33} \end{bmatrix}$, and $\Delta_3 = -\begin{bmatrix} a_{11} & a_{12} & a_{10} \\ a_{21} & a_{22} & a_{20} \\ a_{31} & a_{32} & a_{30} \end{bmatrix}$.

The unknown coefficients for the arch ring can be solved based on the knowledge of structural mechanics. The basic structure of the arch ring under the unit loads $X_i = 1\,(i = 1, 2, 3)$ is shown in Figure 3. The internal forces of the arch ring corresponding to the unit loads $X_1 = 1$, $X_2 = 1$, and $X_3 = 1$ are presented in the following equations, respectively:

$$\begin{cases} M_1 = 1, \\ N_1 = 0, \\ Q_1 = 0, \end{cases} \tag{8}$$

$$\begin{aligned}
&\text{left half arch ring:} \begin{cases} M_2 = R(1 - \cos\varphi_i), \\ N_2 = \cos\varphi_i, \\ Q_2 = -\sin\varphi_i, \end{cases} \\
&\text{right half arch ring:} \begin{cases} M_2 = R(1 - \cos\varphi_i), \\ N_2 = \cos\varphi_i, \\ Q_2 = \sin\varphi_i, \end{cases}
\end{aligned} \tag{9}$$

$$\begin{aligned}
&\text{left half arch ring:} \begin{cases} M_3 = -R\sin\varphi_i, \\ N_3 = \sin\varphi_i, \\ Q_3 = \cos\varphi_i, \end{cases} \\
&\text{right half arch ring:} \begin{cases} M_3 = R\sin\varphi_i, \\ N_3 = -\sin\varphi_i, \\ Q_3 = \cos\varphi_i. \end{cases}
\end{aligned} \tag{10}$$

Since the effect of axial and shear forces on displacement is relatively small, usually only the effect of the bending moments is considered [27]. However, in order to fully consider the internal forces, the axial and shear forces are also involved. According to the structure mechanics, the flexibility coefficients δ_{ij} for the arch ring can be calculated as follows:

$$\delta_{ij} = \sum \int \frac{M_iM_j}{E'I}\,\mathrm{d}s + \sum \int \frac{N_iN_j}{E'A}\,\mathrm{d}s + \sum \int \frac{kQ_iQ_j}{GA}\,\mathrm{d}s, \tag{11}$$

where $M_i\,(M_j)$, $N_i\,(N_j)$, and $Q_i\,(Q_j)$ are the bending moments, axial force, and shear force of the arch ring under the unit loads $X_i\,(X_j) = 1\,(i, j = 1, 2, 3)$ at the crown of the arch ring of the basic structure; E' is the elastic modulus of the arch ring; G is the shear modulus of the arch ring; I is the polar moment of inertia of the arch ring's cross section with respect to the longitudinal direction; A is the area of the cross section; k is the nonuniform coefficient of the shear stress, which is taken as 1.2 for the rectangular cross section in this paper; and s is the arch length.

Substituting equations (8)–(10) into equation (11) for i, $j = 1,2,3$, respectively, the flexibility coefficients of the left tunnel can be obtained as follows:

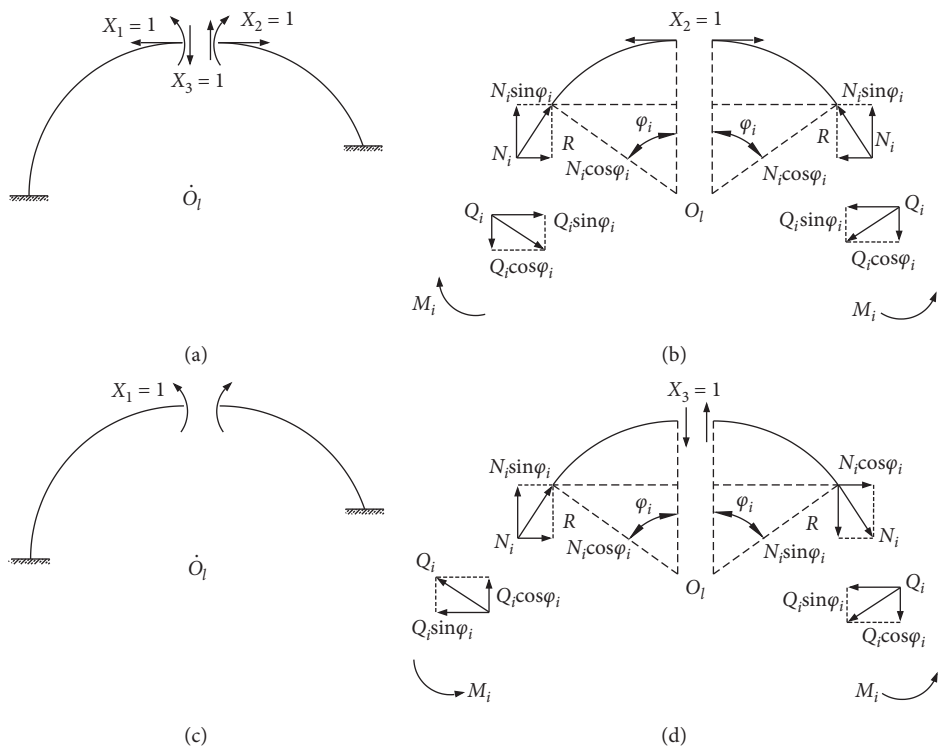

Figure 3: The basic structure of the arch ring under the unit load.

$$
\left.
\begin{aligned}
&\delta_{11} = \frac{R}{EI}\left(\varphi_h + \varphi_d\right) \\
&\delta_{22} = \frac{R_3}{EI}\left[\frac{3}{2}\left(\varphi_h + \varphi_d\right) - 2\left(\sin\varphi_h + \sin\varphi_d\right) + \frac{1}{4}\left(\sin 2\varphi_h + \sin 2\varphi_d\right)\right] \\
&+\left(\frac{R}{EA} + \frac{kR}{GA}\right)\frac{1}{2}\left(\varphi_h + \varphi_d\right) + \left(\frac{R}{EA} - \frac{kR}{GA}\right)\frac{1}{4}\left(\sin 2\varphi_h + \sin 2\varphi_d\right) \\
&\delta_{33} = \left(\frac{R^3}{EI} + \frac{R}{EA}\right)\left[\frac{1}{2}\left(\varphi_h + \varphi_d\right) - \frac{1}{4}\left(\sin 2\varphi_h + \sin 2\varphi_d\right)\right] \\
&+\frac{kR}{GA}\left[\frac{1}{2}\left(\varphi_h + \varphi_d\right) + \frac{1}{4}\left(\sin 2\varphi_h + \sin 2\varphi_d\right)\right] \\
&\delta_{12} = \delta_{21} = \frac{R^2}{EI}\left[\left(\varphi_h + \varphi_d\right) - \left(\sin\varphi_h + \sin\varphi_d\right)\right] \\
&\delta_{13} = \delta_{31} = \frac{R^2}{EI}\left(\cos\varphi_h - \cos\varphi_d\right) \\
&\delta_{23} = \delta_{32} = \frac{R^3}{EI}\left[\left(\cos\varphi_h - \cos\varphi_d\right) + \frac{1}{4}\left(\cos 2\varphi_d - \cos 2\varphi_h\right)\right] \\
&+\left(\frac{kR}{4GA} - \frac{R}{4EA}\right)\left(\cos 2\varphi_h - \cos 2\varphi_d\right)
\end{aligned}
\right\}. \tag{12}
$$

Note that φ_i ranges from 0 to φ_h for the left half arch ring and 0 to φ_d for the right half arch ring. The flexibility coefficients of the right tunnel can be obtained by replacing φ_h and φ_d by φ_d' and φ_h' in the same formulae of the left tunnel.

The internal forces caused by active pressures can be determined by accumulating the pressures as shown in Figure 4, namely, the vertical uniform pressure q, the vertical triangular pressure q', and the lateral trapezoidal pressure $e + \Delta e$ at both sides which can be considered as uniform pressures $e = e_1$ for the left half arch ring and $e = e_1'$ for the right half arch ring with the triangular pressure $\Delta e = f_1 \tan\alpha_1$ for the left half arch ring and $\Delta e = f_2 \tan\alpha_2$ for the right half ring.

$$\begin{cases} M_{ip}^o = M_{iq}^o + M_{iq'}^o + M_{ie}^o + M_{i\Delta e}^o, \\ N_{ip}^o = N_{iq}^o + N_{iq'}^o + N_{ie}^o + N_{i\Delta e}^o, \\ Q_{ip}^o = Q_{iq}^o + Q_{iq'}^o + Q_{ie}^o + Q_{i\Delta e}^o, \end{cases} \tag{13}$$

where M_{ip}^o, N_{ip}^o, and Q_{ip}^o denote the bending moment, axial force, and shear force under the active pressures, respectively.

For the vertical uniform pressure q,

$$\begin{aligned} &\text{left half arch ring}: \begin{cases} M_{iq}^o = -\dfrac{1}{2} q R^2 \sin^2\varphi_i, \\ N_{iq}^o = qR\sin^2\varphi_i, \\ Q_{iq}^o = Rq\sin\varphi_i\cos\varphi_i, \end{cases} \\ &\text{right half arch ring}: \begin{cases} M_{iq}^o = -\dfrac{1}{2} q R^2 \sin^2\varphi_i, \\ N_{iq}^o = qR\sin^2\varphi_i, \\ Q_{iq}^o = -qR\sin\varphi_i\cos\varphi_i. \end{cases} \end{aligned} \tag{14}$$

For the vertical triangular pressure q',

$$\begin{cases} M_{iq'}^o = -\dfrac{1}{6} R^3 \tan\alpha_3 \cdot \sin^3\varphi_i, \\ N_{iq'}^o = \dfrac{1}{2} R^2 \tan\alpha_3 \cdot \sin^3\varphi_i, \\ Q_{iq'}^o = -\dfrac{1}{2} R^2 \tan\alpha_3 \cdot \sin^2\varphi_i \cos\varphi_i. \end{cases} \tag{15}$$

For the lateral uniform pressure e,

$$\begin{aligned} &\text{left half arch ring}: \begin{cases} M_{ie}^o = -\dfrac{1}{2} e_1 R^2 (1-\cos\varphi_i)^2, \\ N_{ie}^o = -e_1 R\cos\varphi_i (1-\cos\varphi_i), \\ Q_{ie}^o = e_1 R\sin\varphi_i (1-\cos\varphi_i), \end{cases} \\ &\text{right half arch ring}: \begin{cases} M_{ie}^o = -\dfrac{1}{2} e_1' R^2 (1-\cos\varphi_i)^2, \\ N_{ie}^o = -e_1' R\cos\varphi_i (1-\cos\varphi_i), \\ Q_{ie}^o = -e_1' R\sin\varphi_i (1-\cos\varphi_i). \end{cases} \end{aligned} \tag{16}$$

For the triangular pressure Δe,

$$\begin{aligned} &\text{left half arch ring}: \begin{cases} M_{i\Delta e}^o = -\dfrac{1}{6} R^3 \tan\alpha_1 (1-\cos\varphi_i)^3, \\ N_{i\Delta e}^o = -\dfrac{1}{2} R^2 \tan\alpha_1 (1-\cos\varphi_i)^2 \cos\varphi_i, \\ Q_{i\Delta e}^o = \dfrac{1}{2} R^2 \tan\alpha_1 (1-\cos\varphi_i)^2 \sin\varphi_i, \end{cases} \\ &\text{right half arch ring}: \begin{cases} M_{i\Delta e}^o = -\dfrac{1}{6} R^3 \tan\alpha_2 (1-\cos\varphi_i)^3, \\ N_{i\Delta e}^o = -\dfrac{1}{2} R^2 \tan\alpha_2 (1-\cos\varphi_i)^2 \cos\varphi_i, \\ Q_{i\Delta e}^o = -\dfrac{1}{2} R^2 \tan\alpha_2 (1-\cos\varphi_i)^2 \sin\varphi_i. \end{cases} \end{aligned} \tag{17}$$

The displacement coefficients Δ_{ip} for the arch ring can be calculated as follows:

$$\Delta_{ip} = \sum \int \frac{M_i M_p^o}{E'I} \mathrm{d}s + \sum \int \frac{N_i N_p^o}{E'A} \mathrm{d}s + \sum \int \frac{k Q_i Q_p^o}{GA} \mathrm{d}s. \tag{18}$$

Substituting equation (14) and equations (8)–(10) into equation (18) yields the following displacement coefficients of the arch ring under the vertical uniform pressure q:

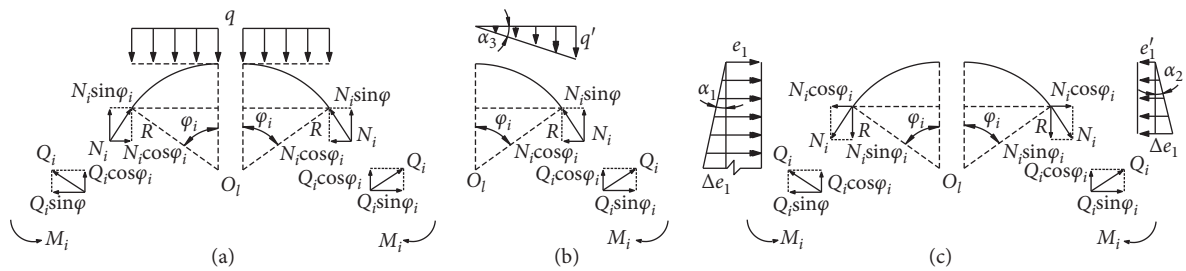

Figure 4: The force analysis diagrams of the basic structure of the arch ring under (a) vertical uniform pressure; (b) vertical triangular pressure; (c) lateral trapezoidal pressure.

$$\left.\begin{aligned}
\Delta_{1q} &= -\frac{R^3 q}{4EI}\left(\varphi_h+\varphi_d\right)+\frac{R^3 q}{8EI}\left(\sin 2\varphi_h+\sin 2\varphi_d\right)\\
\Delta_{2q} &= -\frac{1}{EI}\left\{\begin{array}{c}\frac{1}{4}qR^4\left(\varphi_h+\varphi_d\right)-\frac{1}{8}qR^4\left(\sin 2\varphi_h+\sin 2\varphi_d\right)\\ -\frac{1}{6}qR^4\left(\sin^3\varphi_h+\sin^3\varphi_d\right)\end{array}\right\}+\left(\frac{1}{EA}-\frac{k}{GA}\right)\frac{1}{3}R^2 q\left(\sin^3\varphi_h+\sin^3\varphi_d\right)\\
\Delta_{3q} &= \frac{1}{EI}\left[\frac{1}{2}qR^4\left(\cos\varphi_d-\cos\varphi_h\right)+\frac{1}{6}qR^4\left(\cos^3\varphi_h-\cos^3\varphi_d\right)\right]\\
&+\frac{1}{EA}\left[qR^2\left(\cos\varphi_d-\cos\varphi_h\right)+\frac{1}{3}qR^2\left(\cos^3\varphi_h-\cos^3\varphi_d\right)\right]\\
&+\frac{k}{GA}\frac{1}{3}qR^2\left(\cos^3\varphi_d-\cos^3\varphi_h\right)
\end{aligned}\right\}. \tag{19}$$

Using the same method, the corresponding displacement coefficients for other active pressures can be obtained as follows:

$$\left.\begin{aligned}
\Delta_{1q'} &= \frac{R^4\tan\alpha_3}{6EI}\left(\cos\varphi_d-\frac{1}{3}\cos^3\varphi_d-\frac{2}{3}\right)\\
\Delta_{2q'} &= \frac{R^5\tan\alpha_3}{6EI}\left(\cos\varphi_d-\frac{1}{3}\cos^3\varphi_d-\frac{2}{3}+\frac{1}{4}\sin^4\varphi_d\right)\\
&+\frac{R^3\tan\alpha_3}{8EA}\sin^4\varphi_d-\frac{kR^3\tan\alpha_3}{8GA}\sin^4\varphi_d\\
\Delta_{3q'} &= -\left(\frac{R^5\tan\alpha_3}{6EI}+\frac{R^3\tan\alpha_3}{2EA}\right)\left(\frac{3}{8}\varphi_d-\frac{1}{4}\sin 2\varphi_d+\frac{1}{32}\sin 4\varphi_d\right)\\
&-\frac{kR^3\tan\alpha_3}{2GA}\left(\frac{1}{8}\varphi_d-\frac{1}{32}\sin 4\varphi_d\right)
\end{aligned}\right\}.$$

$$\Delta_{1e} = -\left[\frac{3R^3}{4EI}\left(e_1\varphi_h + e_1'\varphi_d\right) - \frac{R^3}{EI}\left(e_1\sin\varphi_h + e_1'\sin\varphi_d\right) + \frac{R^3}{8EI}\left(e_1\sin 2\varphi_h + e_1'\sin 2\varphi_d\right)\right],$$

$$\Delta_{2e} = -\frac{R^4}{2EI}\left[\begin{array}{c}\frac{5}{4}\left(e_1\varphi_h + e_1'\varphi_d\right) - 4\left(e_1\sin\varphi_h + e_1'\sin\varphi_d\right) + \frac{3}{4}\left(e_1\sin 2\varphi_h + e_1'\sin 2\varphi_d\right)\\ +\frac{1}{3}\left(e_1\sin^3\varphi_h + e_1'\sin^3\varphi_d\right)\end{array}\right]$$

$$-\frac{R^2}{EA}\left[\begin{array}{c}\frac{1}{2}\left(e_1\varphi_h + e_1'\varphi_d\right) - \left(e_1\sin\varphi_h + e_1'\sin\varphi_d\right)\\ +\frac{1}{4}\left(e_1\sin 2\varphi_h + e_1'\sin 2\varphi_d\right) + \left(e_1\sin^3\varphi_h + e_1'\sin^3\varphi_d\right)\end{array}\right] - \frac{kR^2}{GA}\left[\begin{array}{c}\frac{1}{2}\left(e_1\varphi_h + e_1'\varphi_d\right)\Big\}\\ -\frac{1}{4}\left(e_1\sin 2\varphi + e_1'\sin 2\varphi_d\right) - \frac{1}{3}\left(e_1\sin^3\varphi_h + e_1'\sin^3\varphi_d\right)\end{array}\right],$$

$$\Delta_{3e} = \frac{R^4}{2EI}\left[e_1\frac{\left(1-\cos\varphi_h\right)^3}{3} - e_1'\frac{\left(1-\cos\varphi_d\right)^3}{3}\right]$$

$$+\left(\frac{R^2}{EA} - \frac{kR^2}{GA}\right)\left[\frac{1}{2}\left(e_1\cos^2\varphi_h - e_1'\cos^2\varphi_d\right) + \frac{1}{3}\left(e_1'\cos^3\varphi_h - e_1\cos^3\varphi_d\right)\right],$$

$$\left.\begin{array}{l}
\Delta_{1\Delta e} = -\frac{R^4}{6EI}\left[\begin{array}{c}\frac{5}{2}\left(\varphi_h\tan\alpha_1 + \varphi_d\tan\alpha_1\right) - 4\left(\tan\alpha_1\sin\varphi_h + \tan\alpha_2\sin\varphi_d\right)\\ +\frac{3}{4}\left(\tan\alpha_1\sin 2\varphi_h + \tan\alpha_2\sin 2\varphi_d\right) + \frac{1}{3}\left(\tan\alpha_1\sin^3\varphi_h + \tan\alpha_2\sin^3\varphi_d\right)\end{array}\right]\\
\Delta_{2\Delta e} = -\frac{R^5}{6EI}\left[\begin{array}{c}\frac{35}{8}\left(\varphi_h\tan\alpha_1 + \varphi_d\tan\alpha_2\right) - 8\left(\tan\alpha_1\sin\varphi_h + \tan\alpha_2\sin\varphi_d\right)\\ +\frac{7}{4}\left(\tan\alpha_1\sin 2\varphi_h + \tan\alpha_2\sin 2\varphi_d\right) + \frac{4}{3}\left(\tan\alpha_1\sin^3\varphi_h + \tan\alpha_2\sin^3\varphi_d\right)\\ +\frac{1}{32}\left(\tan\alpha_1\sin 4\varphi_h + \tan\alpha_2\sin 4\varphi_d\right)\end{array}\right]\\
-\frac{R^3}{2EA}\left[\begin{array}{c}\frac{7}{8}\left(\varphi_h\tan\alpha_1 + \varphi_d\tan\alpha_2\right) + \frac{1}{2}\left(\tan\alpha_1\sin 2\varphi_k + \tan\alpha_2\sin 2\varphi_d\right)\\ +\frac{2}{3}\left(\tan\alpha_1\sin^3\varphi_h + \tan\alpha_2\sin^3\varphi_d\right) + \frac{1}{32}\left(\tan\alpha_1\sin 4\varphi_h + \tan\alpha_2\sin 4\varphi_d\right)\end{array}\right]\\
-\frac{kR^3}{2GA}\left[\begin{array}{c}\frac{5}{8}\left(\varphi_h\tan\alpha_1 + \varphi_d\tan\alpha_2\right) - \frac{1}{4}\left(\tan\alpha_1\sin 2\varphi_h + \tan\alpha_2\sin 2\varphi_d\right)\\ -\frac{2}{3}\left(\tan\alpha_1\sin^3\varphi_h + \tan\alpha_2\sin^3\varphi_d\right) - \frac{1}{32}\left(\tan\alpha_1\sin 4\varphi_h + \tan\alpha_2\sin 4\varphi_d\right)\end{array}\right]\\
\Delta_{3\Delta e} = \frac{R^5}{6EI}\left[\begin{array}{c}\left(\cos\varphi_d\tan\alpha_2 - \cos\varphi_h\tan\alpha_1\right) + \frac{3}{2}\left(\cos^2\varphi_h\tan\alpha_1 - \cos^2\varphi_d\tan\alpha_2\right)\\ +\left(\cos^3\varphi_d\tan\alpha_2 - \cos^3\varphi_h\tan\alpha_1\right) + \frac{1}{4}\left(\cos^4\varphi_h\tan\alpha_1 - \cos^4\varphi_d\tan\alpha_2\right)\end{array}\right]\\
+\left(\frac{R^3}{2EA} - \frac{kR^3}{2GA}\right)\left[\begin{array}{c}\frac{1}{2}\left(\cos^2\varphi_h\tan\alpha_1 - \cos^2\varphi_d\tan\alpha_2\right)\\ -\frac{2}{3}\left(\cos^3\varphi_h\tan\alpha_1 - \cos^3\varphi_d\tan\alpha_2\right) + \frac{1}{4}\left(\cos^4\varphi_h\tan\alpha_1 - \cos^4\varphi_d\tan\alpha_2\right)\end{array}\right]
\end{array}\right\}. \tag{20}$$

The displacement coefficients under the active pressures are the superposition of the obtained coefficients, which can be expressed by the following:

$$\left.\begin{aligned}\Delta_{1p} &= \Delta_{1q} + \Delta_{1q'} + \Delta_{1e} + \Delta_{1\Delta e}\\ \Delta_{2p} &= \Delta_{2q} + \Delta_{2q'} + \Delta_{2e} + \Delta_{2\Delta e}\\ \Delta_{3p} &= \Delta_{3q} + \Delta_{3q'} + \Delta_{3e} + \Delta_{3\Delta e}\end{aligned}\right\}. \tag{21}$$

Accordingly, the displacement coefficients for the right tunnel can be obtained by utilizing the same method.

After the coefficients for the arch ring have been obtained, the remaining unknown coefficients at the top of the side wall and middle wall could be calculated by the elastic beam model and the force analysis on the top of the middle wall, which are shown in Appendix A and B, respectively.

Based on the obtained coefficients, the redundant forces X_{1p}, X_{2p}, and X_{3p} can be obtained by equation (7). Based on equation (7), the internal forces along the arch ring can be determined according to the static equilibrium condition, which are given by equations (22) and (23) for the left and right half arch rings, respectively. The bending moment M_{ia} is positive when the intrados of the arch ring is in tension and the axial force N_{ia} is positive when the arch ring is under compression, while the shear force Q_{ia} leading to the clockwise rotation of the arch section is taken as positive.

$$\begin{cases} M_{ia} = X_{1p} + X_{2p}y_i - X_{3p}x_i + M_{ip}^o,\\ N_{ia} = X_{2p}\cos\varphi_i + X_{3p}\sin\varphi_i + N_{ip}^o,\\ Q_{ia} = -X_{2p}\sin\varphi_i + X_{3p}\cos\varphi_i + Q_{ip}^o,\end{cases} \tag{22}$$

$$\begin{cases} M_{ia} = X_{1p} + X_{2p}y_i - X_{3p}x_i + M_{ip}^o,\\ N_{ia} = X_{2p}\cos\varphi_i + X_{3p}\sin\varphi_i + N_{ip}^o,\\ Q_{ia} = -X_{2p}\sin\varphi_i + X_{3p}\cos\varphi_i + Q_{ip}^o,\end{cases} \tag{23}$$

where M_{ip}^o, N_{ip}^o, and Q_{ip}^o are the internal forces for arbitrary positions of the arch ring subject to the active pressures and φ_i is the angle between the analysed cross section and crown of the arch ring, which is in the range of $0\sim\varphi_h$ for the left half arch ring and $0\sim\varphi_d$ for the right half arch ring.

Because of symmetry and by using the same methods, the analytical solutions of internal forces for the right tunnel arch ring can be obtained accordingly.

3.2. Analytical Solutions for the Side Wall. The internal forces of the arch rings are transferred continuously to the side wall through the arch foot, as shown in Figure 5(a). For the side wall, the bending moment M_{is} is positive when the intrados of the side wall is in tension and the axial force N_{is} is positive when the side wall is under compression, while the shear force Q_{is} leading to the clockwise rotation of the side wall is positive.

In general, the angle of the joint of the side wall and arch foot at the crown of the arch ring, namely, φ_h for the left tunnel and φ_h' for the right one, are usually right angle and it is unnecessary to decompose the internal forces. Nevertheless, in order to embrace more general situations, φ_h and φ_h' are considered to be arbitrary angles in the current derivation. The corresponding decompositions of the internal forces at the top of the side wall are shown in Figure 5(b).

In the derivation of the analytical solutions, the side wall is assumed to be an elastic foundation beam. The internal forces induced by the unit bending moment, unit horizontal force, and vertical force exerted on the top of the side wall are first derived separately, which can refer to Appendix A. The real internal forces are obtained by applying the principle of superposition. For the left tunnel, the final solutions for the internal forces of the side wall are obtained as follows:

$$\begin{cases} M_{is} = M_h M_{M=1} + (-Q_h\sin\varphi_h + N_h\cos\varphi_h)M_{H=1}\\ \quad + (Q_h\cos\varphi_h + N_h\sin\varphi_h)M_{V=1} + M_e + M_{\Delta e},\\ Q_{is} = M_h Q_{M=1} + (-Q_h\sin\varphi_h + N_h\cos\varphi_h)Q_{H=1}\\ \quad + (Q_h\cos\varphi_h + N_h\sin\varphi_h)\cdot Q_{V=1} + Q_e + Q_{\Delta e},\\ N_{is} = Q_h\cos\varphi_h + N_h\sin\varphi_h,\end{cases} \tag{24}$$

where $M_{M=1}$ and $Q_{M=1}$, $M_{H=1}$ and $Q_{H=1}$, and $M_{V=1}$ and $Q_{V=1}$ are the bending moments and shear forces of the side wall induced by the unit bending moment exerted on the top of the side wall, induced by the unit horizontal force exerted on the top of the sidewall, and induced by the unit vertical force exerted on the top of the sidewall, respectively. M_e and Q_e; $M_{\Delta e}$ and $Q_{\Delta e}$ are the bending moments and shear forces induced by the uniform pressure exerted on the side wall along the vertical direction and induced by the triangular pressure exerted on the side wall along the vertical direction, respectively. They are all related with the elastic resistance according to the elastic foundation beam method, with the derivation given in Appendix A.

The analytical solutions of internal forces for the right tunnel side wall can be obtained in a similar way.

3.3. Analytical Solutions for the Middle Wall. The middle wall is assumed as a cantilever beam. The internal forces of the arch rings are transferred continuously to the middle wall through the arch feet connected with the middle wall. The bending moment M_{im} causing the counterclockwise rotation of the middle wall is positive, the shear force Q_{im} leading the middle wall to rotate clockwise is positive, and the compressive axial force N_{im} is positive. The forces at the top of the middle wall and their decomposition are shown in Figure 6(a).

Based on Figure 6, the analytical solutions of internal forces for the middle wall can be obtained as follows:

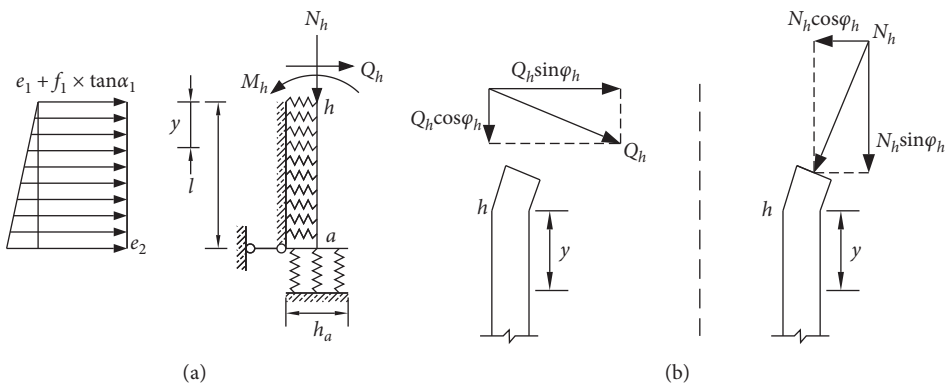

Figure 5: The internal forces on the left side wall: (a) forces transferred to the top of the side wall; (b) the decomposition of the internal forces at the top of the side wall.

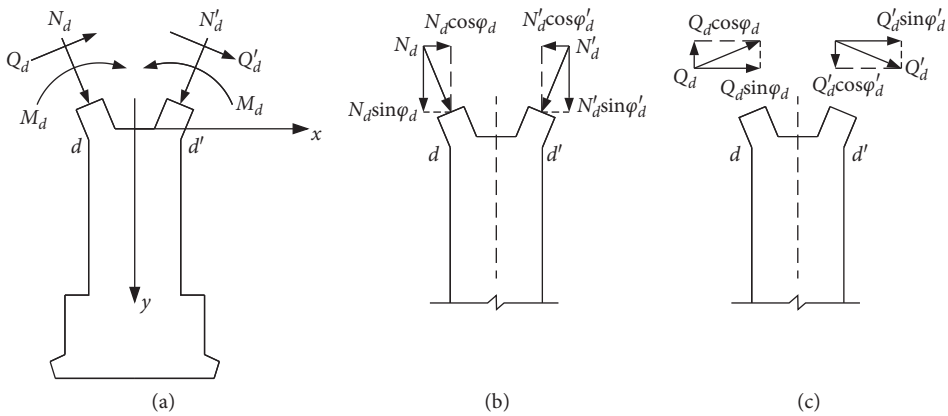

Figure 6: The forces and decompositions at the top of the middle wall.

$$\begin{cases} M_{im} = M_{d'} - M_d - (Q_d \sin\varphi_d + Q_{d'} \sin\varphi_{d'})y_i + (N_{d'} \cos\varphi_{d'} - N_d \cos\varphi_d)y_i, \\ N_{im} = N_d \sin\varphi_d + N_{d'} \sin\varphi_{d'} - Q_d \cos\varphi_d + Q_{d'} \cos\varphi_{d'}, \\ Q_{im} = Q_d \sin\varphi_d + Q_{d'} \sin\varphi_{d'} + N_d \cos\varphi_d - N_{d'} \cos\varphi_{d'}, \end{cases} \tag{25}$$

Equations (22) to (25) constitute the complete analytical solutions of the internal forces of shallow double-arched tunnel for the left tunnel and middle wall. Detailed information on how to determine the unknown coefficients is presented in Appendix A and B.

3.4. Main Steps to Determine the Internal Forces of Double-Arched Tunnel. Figure 7 summarizes the stepwise procedure of deducting the internal forces of double-arched tunnel using the analytical solutions derived in the current study:

(1) determination of the outer dimension and lining characteristics of a double-arched tunnel. The outer dimension of the tunnel should be determined according to the geometry design, including the outer radius of arch ring, the height of side and middle walls, the total width of tunnel, as well as the opening angle. The lining characteristics including the lining thickness and properties should also be determined.

(2) determination of the pressures on a double-arched tunnel. Based on the burial depth and geological conditions, the pressures on the double-arched tunnel can be derived according to the information listed in Figure 1 and Table 1.

(3) determination of the flexibility coefficients and displacement coefficients. Based on the aforementioned methods and equations, the flexibility coefficients (equation (12)) and displacement coefficients (equations (19) to (21)) of arch ring can be determined, respectively. The displacement coefficients of the side wall and middle wall can be determined according to the method in Appendix A and B.

(4) determination of the internal forces of the arch ring from equations (22) and (23).

(5) determination of the internal forces of the side wall and middle wall from the equations (24) and (25), respectively.

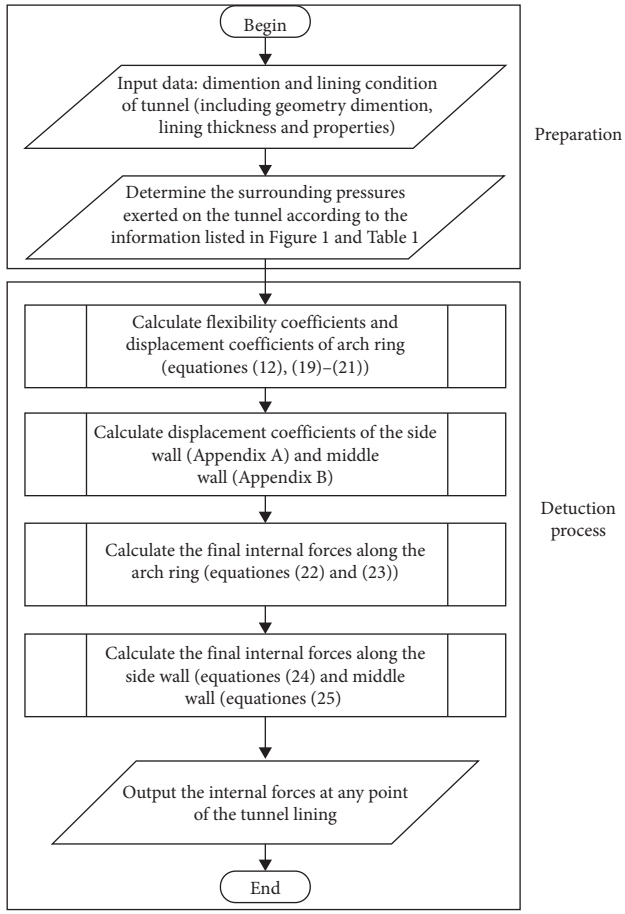

Figure 7: The flow chart of the determining procedures.

Table 3: The main physical and mechanical properties of the grade V surrounding rock [10].

Cohesion (MPa)	Internal friction angle (°)	Elastic modulus (GPa)	Unit weight (kN/m^3)
0.07–0.1	27–29	0.8–1.9	27.5–31.5

The derived analytical solutions in this section mainly focus on the double-arched tunnel subjected to symmetric external loads, while the nonsymmetric scenarios are more commonly encountered in engineering practice. The main differences between the two scenarios are the pressures exerted on the tunnel. For the nonsymmetric ones, the vertical pressures q in Figure 1 will be trapezoidal instead of rectangle; thus, another growth angle of vertical earth pressure α_4 should be added [38], similar to the lateral earth pressure outside of double-arched tunnel. Therefore, the derivation process of displacement coefficients of the arch ring (equations (14) and (19)) should consider the effect of α_4, which is the main difference in the derivation process between the two scenarios. In addition, for deep tunnels, such as the right tunnel, a larger lateral pressure outside the tunnel will be present, and another growth angle α_5 of the lateral pressure may not equal to the present α1 in Figure 1. Nonetheless, the deduced process of the right-side tunnel is still similar to the left one. The remaining part of the deduction of the analytical solution for the nonsymmetric scenarios is the same with the aforementioned process. Overall, it is convenient to extend the present analytical solution to the more common nonsymmetric scenarios.

Table 4: Input information in the analytical solutions.

	Item	Values
Surrounding rock	Equivalent depth H(m)	9.5
	Unit weight γ (kN/m^3)	27.5–31.5
	Elastic modulus E (GPa)	0.8–1.9
	Poisson's ratio μ	0.35–0.45
	Elastic resistance coefficient K(MPa/m)	100–200
	Calculated friction angle φ(°)	40–50
	Friction angle of sliding surface θ (°)	(0.5–0.7) φ
Lining structure	Elastic modulus E' (GPa)	31.75
	Shear modulus G (GPa)	13.65
	Poisson's ratio μ'	0.2
	Unit weight γ'(kN/m^3)	23

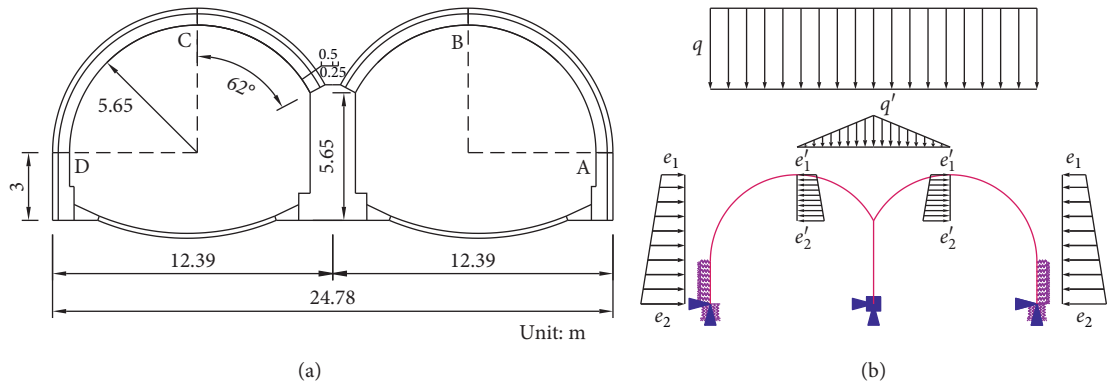

Figure 8: The adopted model of double-arched tunnel: (a) the cross section of the model (adapted from [10]); (b) the 2D FEM model.

4. Model Validation

4.1. Model Overview. As shown in Figure 8(a), the adopted double-arched tunnel model referred to the project introduced by [10]. Since the dimension of the side wall was not clearly defined in [10], for simplicity, the height of the side wall is roughly set to be 3m according to the length scale as presented in [10]. The thickness of the sprayed concrete and the secondary lining is 25 cm and 50 cm, respectively.

The quality of rock mass mainly reflects the pressure exerted on the tunnel lining, which is usually evaluated by the rock mass classification schemes. Over the past decades, a number of rock mass classification schemes have been proposed [39], in which the rock masses are classified into different grades according to their compactness and mechanical properties. For example, the RMR method divides the rock mass into five grades, i.e., grades I ~IV, of which the grade I denotes the rock mass with the highest quality, while the grade V represents the rock mass with the lowest quality. Based on the data available in [10] and according to the design code of China [38], the K89 + 729 section is investigated herein and surrounding rock mass is classified as grade V by the RMR method. The main physical and mechanical properties of the grade V surrounding rock masses are listed in Table 3.

4.2. Input Parameters in the Analytical Solutions. Although the exactly burial depth of the K89 + 729 section was not given in [10], the contact pressures (q) between the surrounding rock and the primary lining at the crown of the arch ring were presented, which equaled to 0.3 MPa. Therefore, the equivalent burial depth (H) of the tunnel section can be back calculated based on Protodyakonov's theory, i.e., $H = q/\gamma = 9.5$ m, which is smaller than the load equivalent height $h_q = 14.24$ m. Then, the detailed information about the ground condition and the secondary lining input in the analytical solutions can be derived as shown in Table 4.

4.3. FEM Numerical Modelling. In order to accurately capture the key characteristics of the elastic foundation beam and the analytical solutions, the load-structure method is adopted in the 2D FEM model. The external pressures exerted on the double-arched tunnel can be calculated using the corresponding values in Table 4 based on the method introduced in Table 1. The determined external pressures will be imported into the load-structure method-based FEM simulations.

All the FEM analyses are carried out under the plane-strain conditions. The numerical model is presented in Figure 8(b), in which the primary lining structure is not considered and the secondary lining is simulated by the beam elements according to the dimensions in Figure 8(a). The extrados and bottom of both side walls are restricted by unidirectional compression springs with a stiffness $K = 200$ MPa/m, which models the elastic resistances from the surrounding rock masses. The bottoms of the side and middle walls are also fixed in both horizontal and vertical directions. The rotation of the middle wall is also inhibited. It should be noted that the FEM model is specified to have the same loading configuration and assumptions of material properties as those adopted for analytical derivations. Therefore, the dynamic ground-structure interaction and plastic yielding of lining structure are not considered.

4.4. Comparison of Results. Figure 9 compares the internal forces derived from analytical solutions and numerical simulations. The variational trend and the distributive pattern of the internal forces of both methods are very close to each other. The discrepancies between the two are overall small and acceptable, except that the bending moment predicted by the analytical solutions deviates increasingly more from the numerical simulation data when approaching the middle wall. This may be because in the analytical solution the elastic resistance coefficient k_d between the top of the middle wall and the arch ring is set to the elastic modulus E' of the lining structure in the analytical solutions. The simplification of beam element of the numerical model at the top of the middle wall may also deviate from the real situation, which may also account for the discrepancies. Further investigations may be required to determine the real contact characteristics at the top of the middle wall for double-arched tunnel.

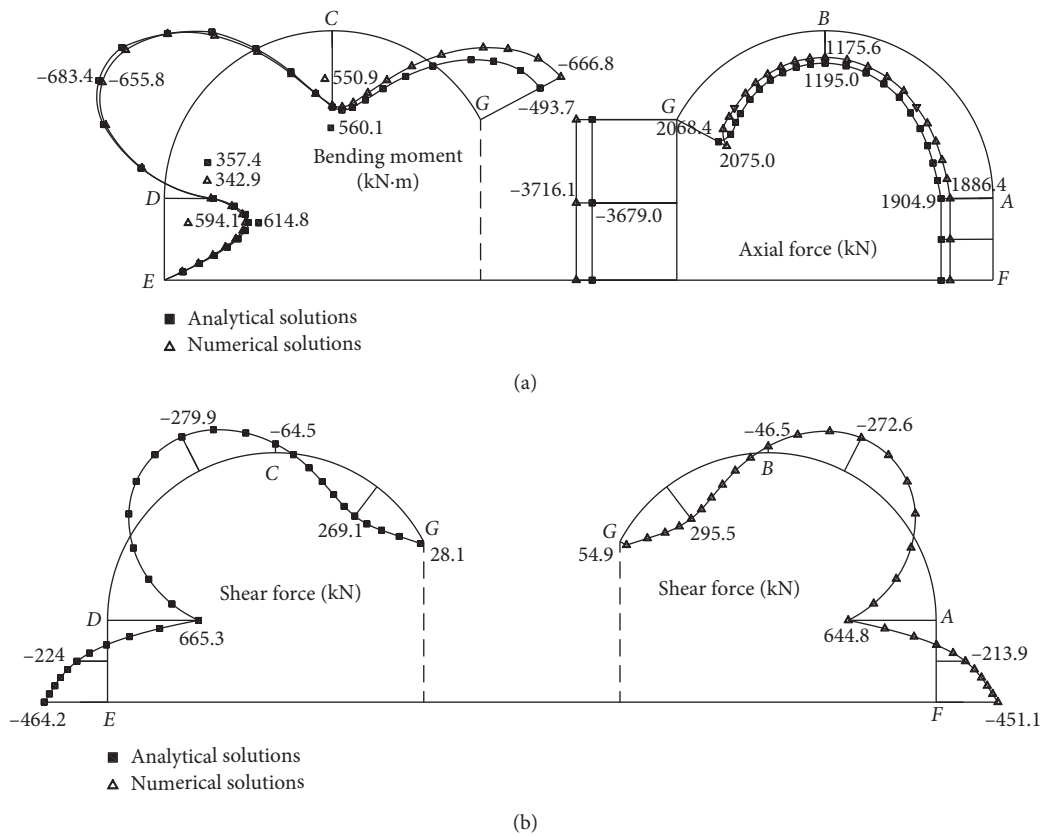

Figure 9: Comparison of the internal forces obtained from the analytical solutions and numerical simulations: (a) bending moment and axial force; (b) shear force.

Despite the discrepancies, the analytical solutions and the numerical solutions are overall in good agreement. It shows that the shear forces are smaller than the axial forces with the maximum shear force located at the conjunction point between the arch ring and the side wall, which is also an inflection point of the shear force distribution. Such an obvious inflection point may be because we only apply the elastic resistance to the side wall. The middle wall only bears the axial forces without presence of bending moment and shear forces in accordance with the symmetry condition of the lining structure and surrounding pressure during the derivation of the analytical solutions.

The distribution law of internal forces can be derived from Figure 9. Specifically, the bending moment in the side wall is positive and increases from the bottom upwards but then decreases when approaching the arch foot. The maximum bending moment of the lining which is in the upper side along the side wall may be caused by the constraint to deformation provided by the external elastic resistance. This is confirmed by Figure 10, which shows that the upper side of the side wall experiences a larger outside deformation than the lower side. The maximum positive bending moment of the arch ring lies near the crown of the arch, and its magnitude is larger than that of the maximum negative bending moment, which is located at the point with an angle about 60° measured from arch crown to the half ring near both side walls. This may also be verified by the deformation shown in Figure 10, of which the larger deformation is present in the crown and outside haunch of both tunnels. The results indicate that both the intrados of the crown and extrados of the haunch of the arch ring are in larger tension. These characteristics should be noted during the design and construction of the tunnel lining structure. Generally, the axial force shows a relatively uniform distribution along the arch ring, while the axial force near the side wall is slightly larger than that near the crown of the arch ring. Thus, the side wall is in larger compression. The smaller axial force near the arch crown may be caused by the larger vertical pressure at the crown, which helps to reduce the axial force in the quasi-horizontal direction. The maximum values of shear force of arch rings in Figure 9(b) mainly appeared near the zero point of bending moment with the nonshear point located close to the place where the maximum bending moment is present, consistent with the general distribution law of forces within beam elements. Furthermore, the large shear force at the bottom of the side wall should be taken into consideration during the design and construction.

5. Parametric Analysis

During the derivation of the analytical solutions, most parameters can be deduced according to the mechanical properties and geometrical characteristics of the lining

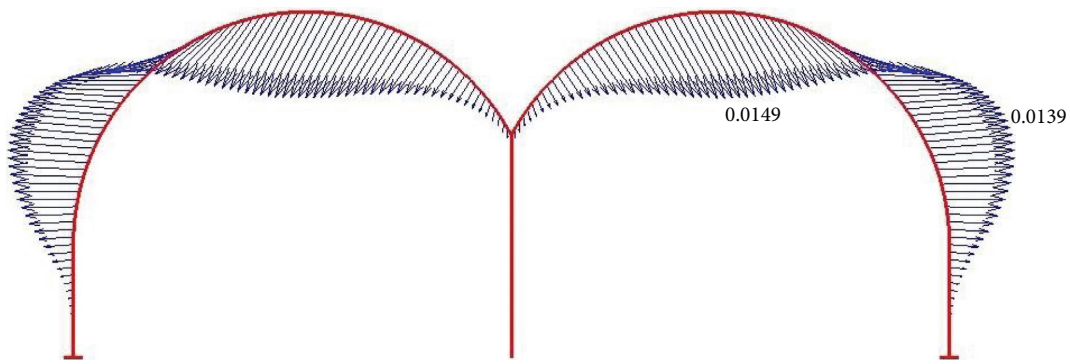

Figure 10: The deformation vector graph of the double-arched tunnel by the FEM analysis.

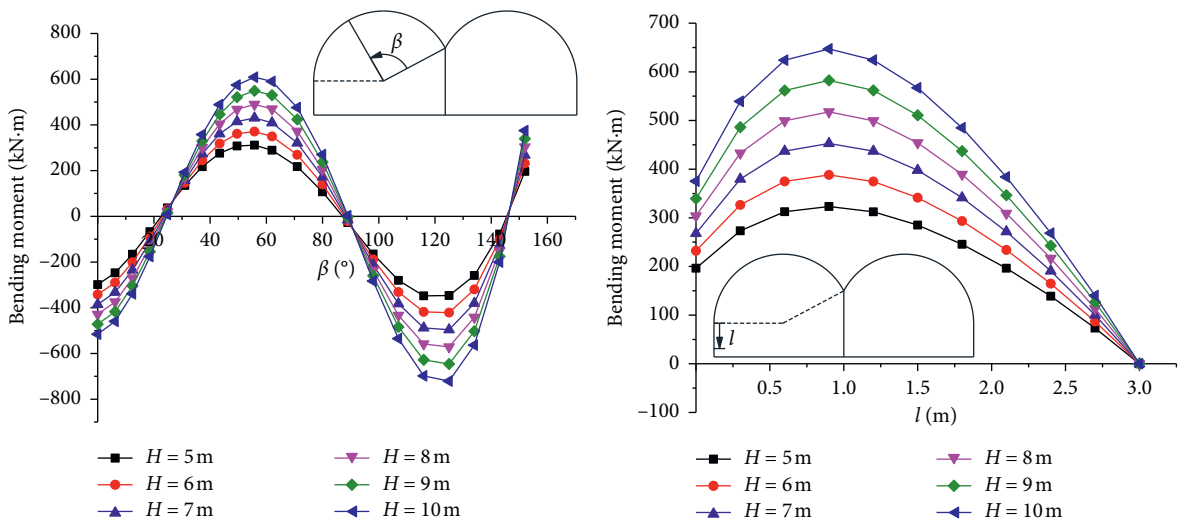

Figure 11: Variations of bending moment with (H): (a) along the arch ring; (b) along the side wall.

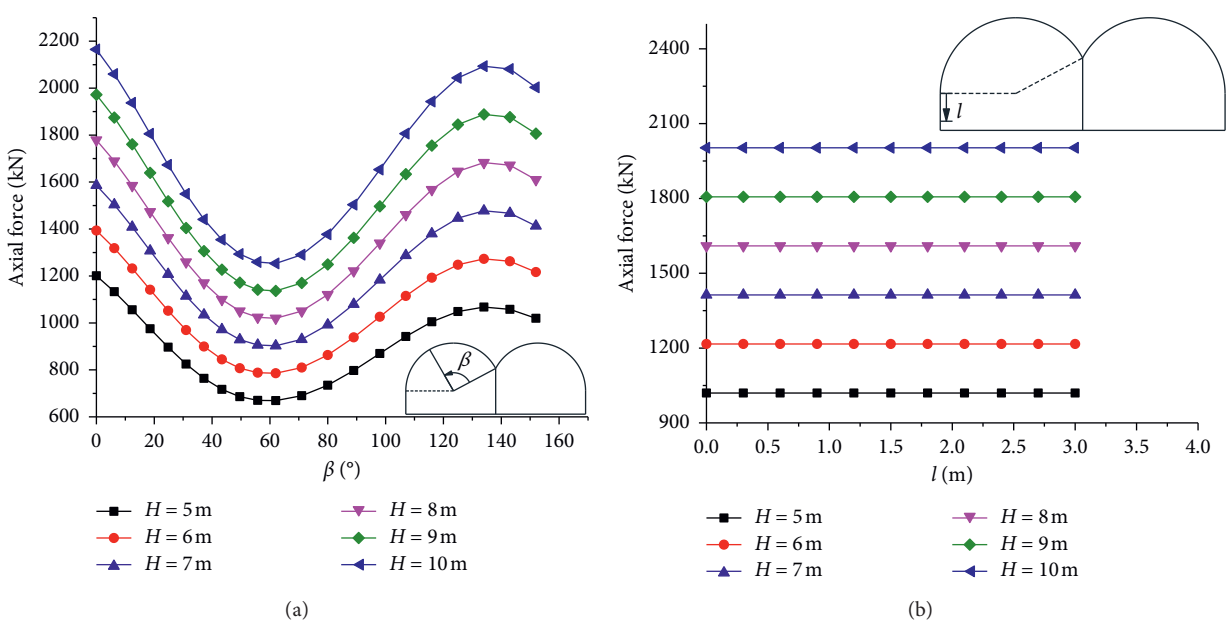

Figure 12: Continued.

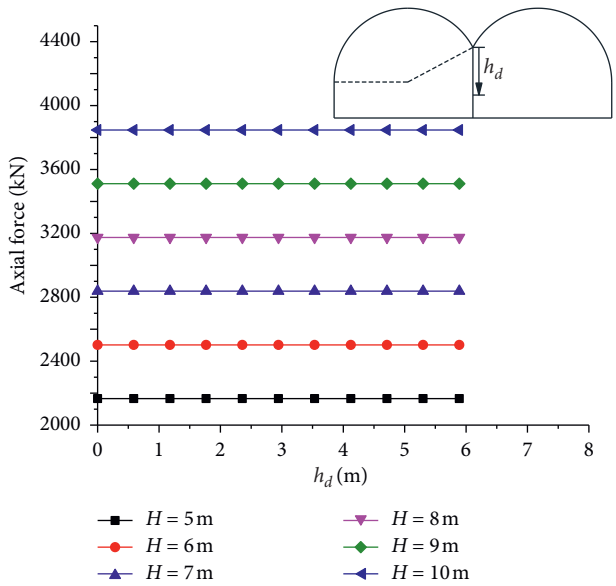

(c)

Figure 12: Variations of axial force with (H): (a) along the arch ring; (b) along the side wall; (c) along the middle wall

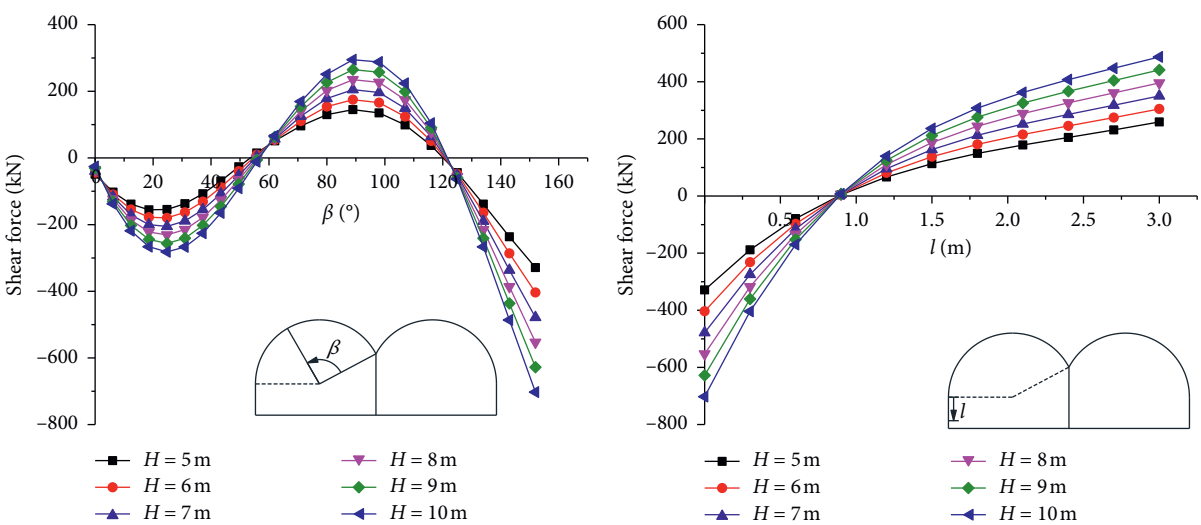

(a) (b)

Figure 13: Variations of shear force with (H): (a) along the arch ring; (b) along the side wall.

structure. However, there are still some factors that cannot be derived directly, such as the real equivalent depth H and the elastic resistance coefficient K of the elastic foundation beam, which may affect the internal force distributions. Furthermore, the opening angle φ_d of the double-arched tunnel is also a main geometrical parameter of the lining structure that may affect the internal force. Besides, to accommodate the increasing transportation demand, the mountain tunnels tend to have large dimensions, while the difference in tunnel span may also change the loading states of the lining structure. Therefore, it is necessary to explore how these factors affect the internal forces and provide useful guidance for the design optimization. In this section, the four factors are varied systematically in the benchmark case presented in the section of Model Validation to investigate their influences on the internal forces. Due to the symmetry of the absolute values, only the internal forces at the left half of the double-arched tunnel are analysed in the following subsections. Note that the shear force on the right half is opposite in sign to that of the left half, while the bending moment and axial force are identical at both sides.

5.1. The Effect of the Burial Depth. The equivalent depth H is varied between 5m and 10m at an increment of 1m.

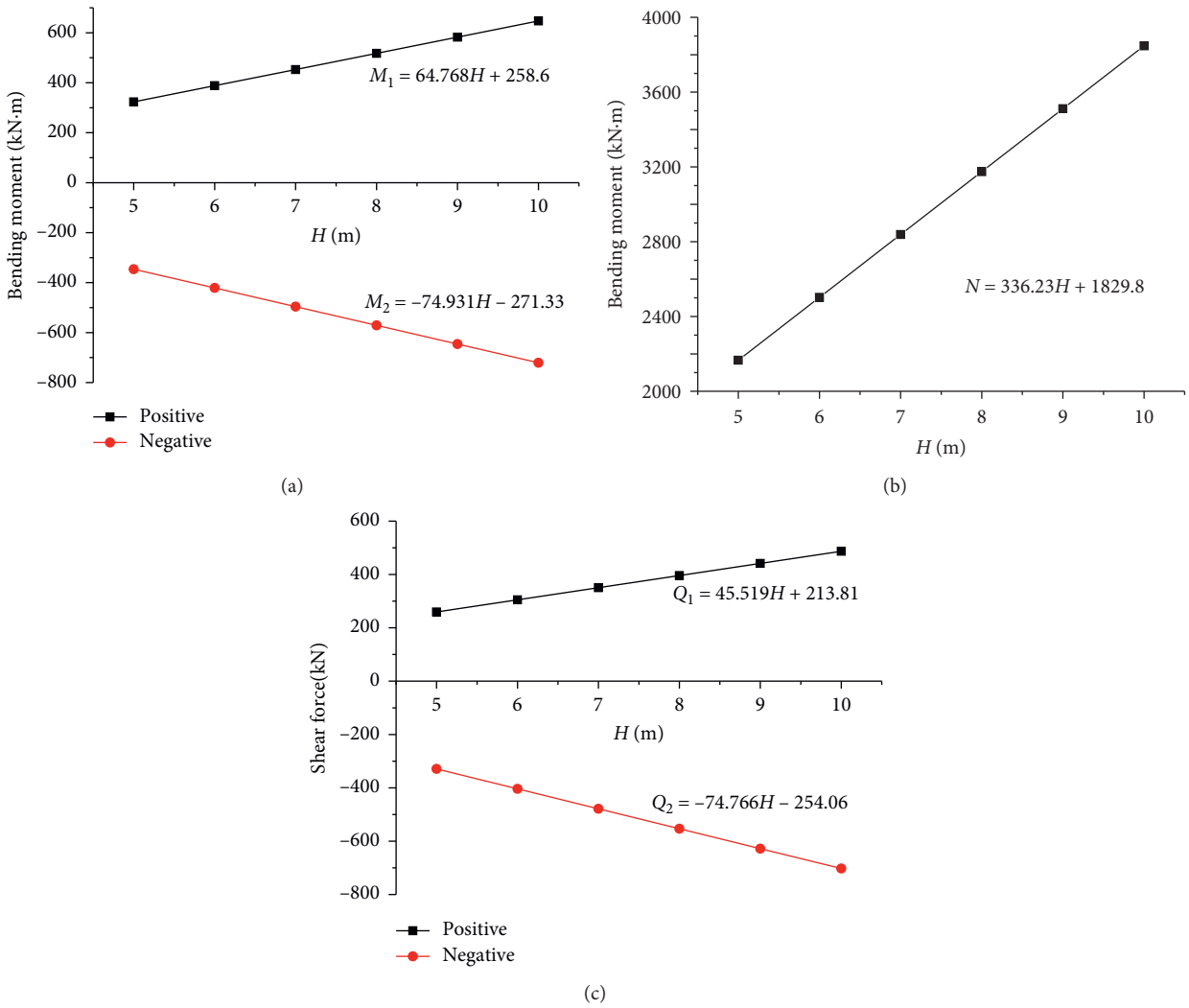

Figure 14: Variations of largest magnitudes of internal forces with (H): (a) bending moment; (b) axial force; (c) shear force.

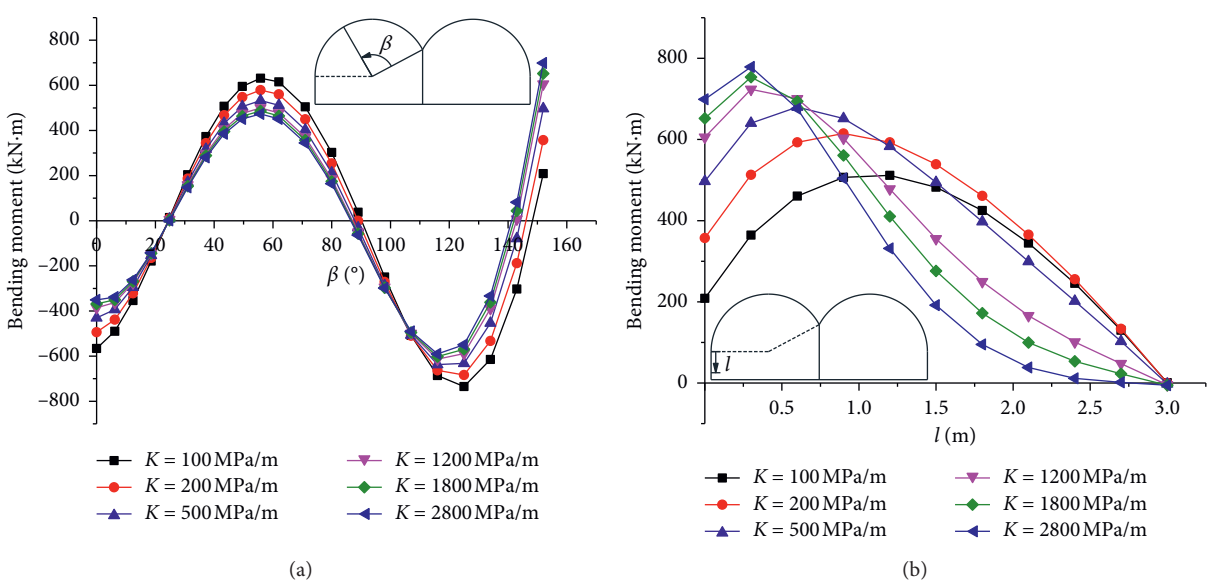

Figure 15: Variations of bending moment with (K): (a) along the arch ring; (b) along the side wall.

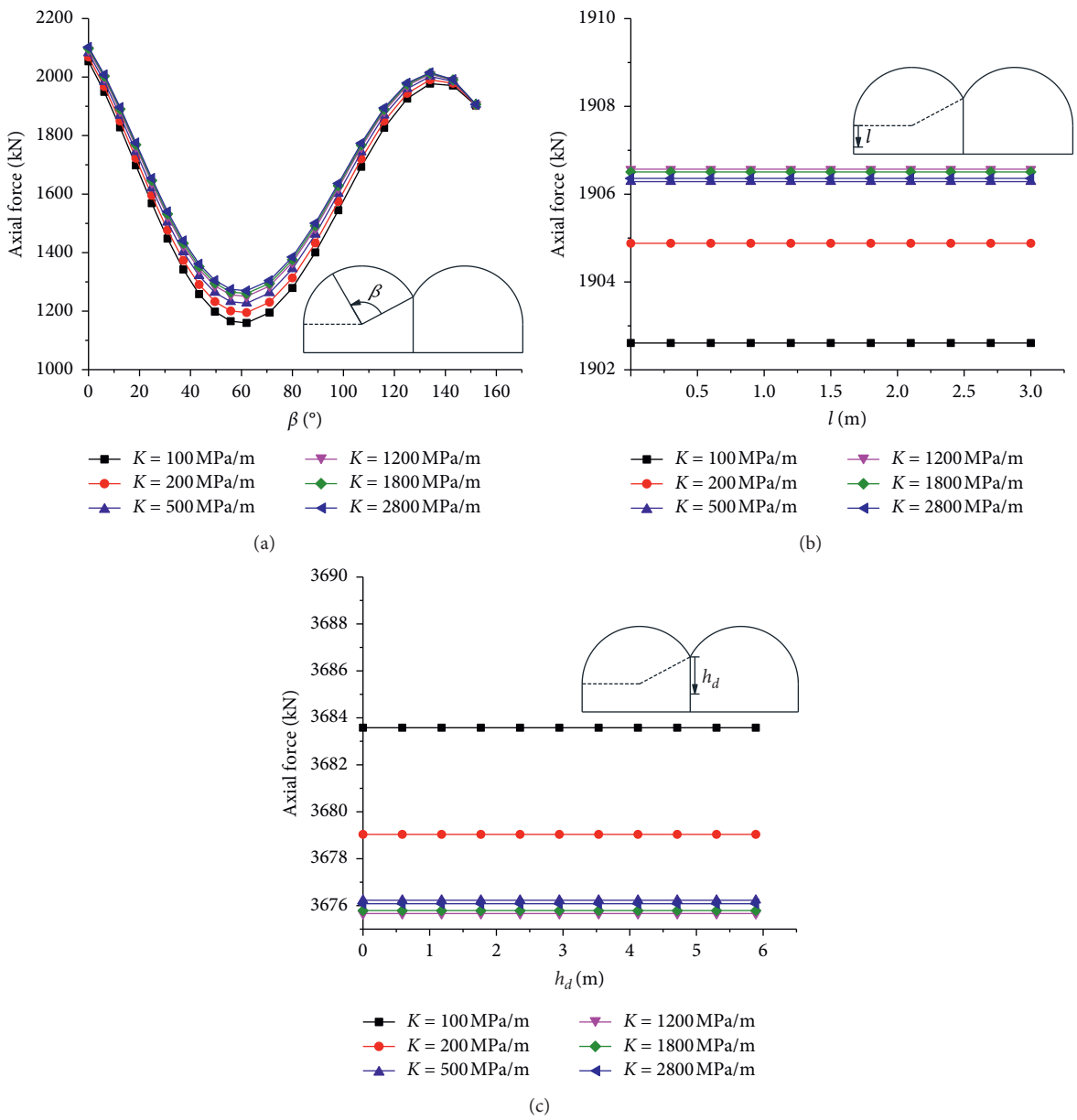

Figure 16: Variations of axial force with (K): (a) along the arch ring; (b) along the side wall; (c) along the middle wall.

Figures 11–13 show the internal forces along the lining structure under different H values. The variation trend and the locations of the maximum and minimum internal forces are independent of H, but the absolute magnitude of the internal forces increases consistently with increasing H.

As shown in Figure 11, the largest positive and negative bending moment are in the side wall about $l = 0.9$ m and the arch ring at location about $\beta = 125^{\circ}$, respectively. The maximum axial force is in the middle wall as shown in Figure 12. The largest shear force occurs at the bottom and top of the side wall as shown in Figure 13. The variations of the largest magnitudes of the internal forces with increasing H are shown in Figure 14, which all show linear correlations. Figure 14 indicates that the internal forces could be significantly affected by the burial depth as expected.

5.2. The Effect of Elastic Resistance Coefficient. The elastic resistance coefficient $K = 200$ MPa/m was adopted in the analytical analysis and FEM analysis presented above for the grade V rock masses. In order to embrace the elastic resistance characteristics of surrounding rock masses with different grades, a wide range of K ($K = 100$, 200, 500, 1200, 1800, and 2800 MPa/m) is adopted in this section which may represent the grade I~V rock masses. Figures 15–17 show the internal forces along the lining structure under different elastic resistance coefficients.

The magnitude of bending moment along the arch ring decreases with the increasing K except the section near the top of the side wall which becomes larger as K increases. The bending moment along the side wall increases as K increases from 100 to 200 MPa/m. When K is greater than 500 MPa/m, the bending moment initially increases with the increasing K

Table 5: Geometrical parameters corresponding to different opening angles φ_d.

φ_d (°)	f_2 (m)	h_d (m)	B(m)
35	1.11	8.04	19.35
45	1.80	7.35	21.00
55	2.62	6.53	22.38
65	3.55	5.60	23.45
75	4.56	4.59	24.18

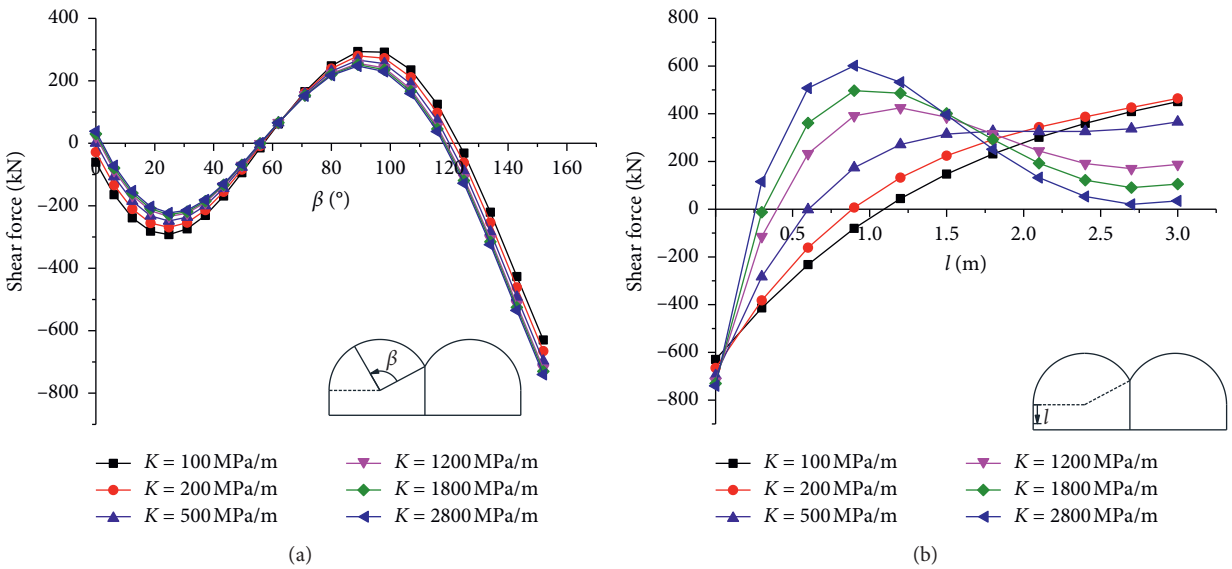

Figure 17: Variations of shear force with (K): (a) along the arch ring; (b) along the side wall.

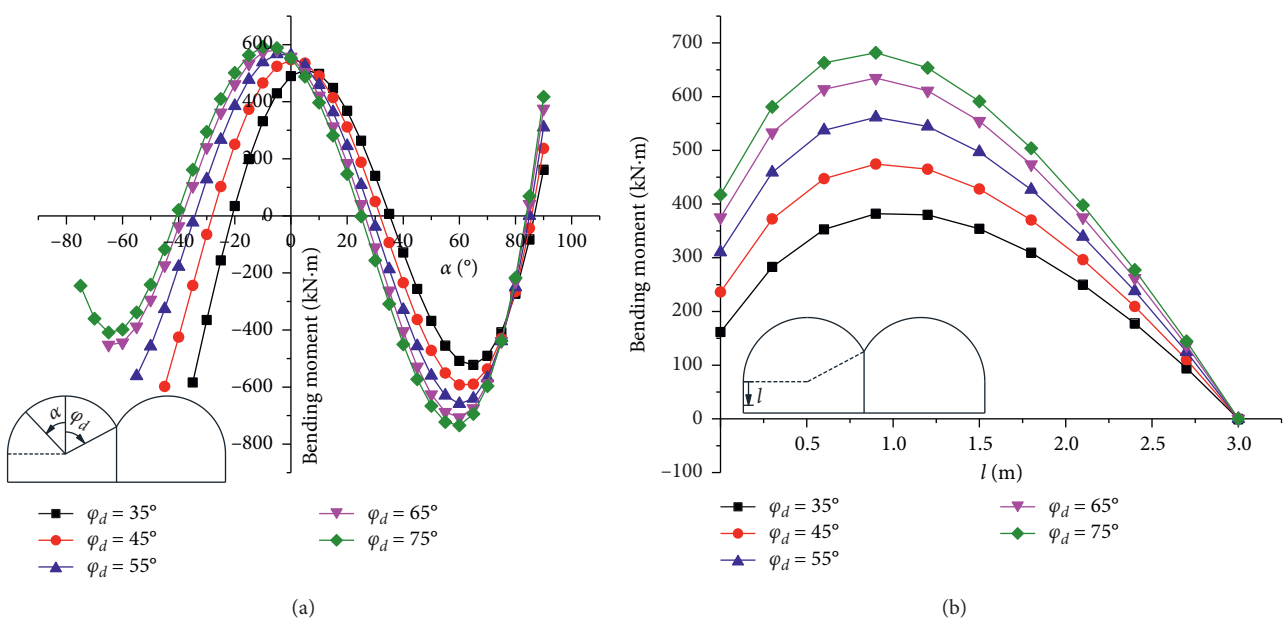

Figure 18: Variations of bending moment with φ_d: (a) along the arch ring; (b) along the side wall.

for the top fifth of the side wall and then decreases as K increases for the remaining section of the side wall. The axial force along the arch ring initially decreases with increasing K but becomes approximately constant as K reaches 1200 MPa/m. The axial force along the side wall increases and the axial force along the middle wall decreases with increasing K, but their changes in magnitude are negligible. The magnitude of the shear force along the arch ring

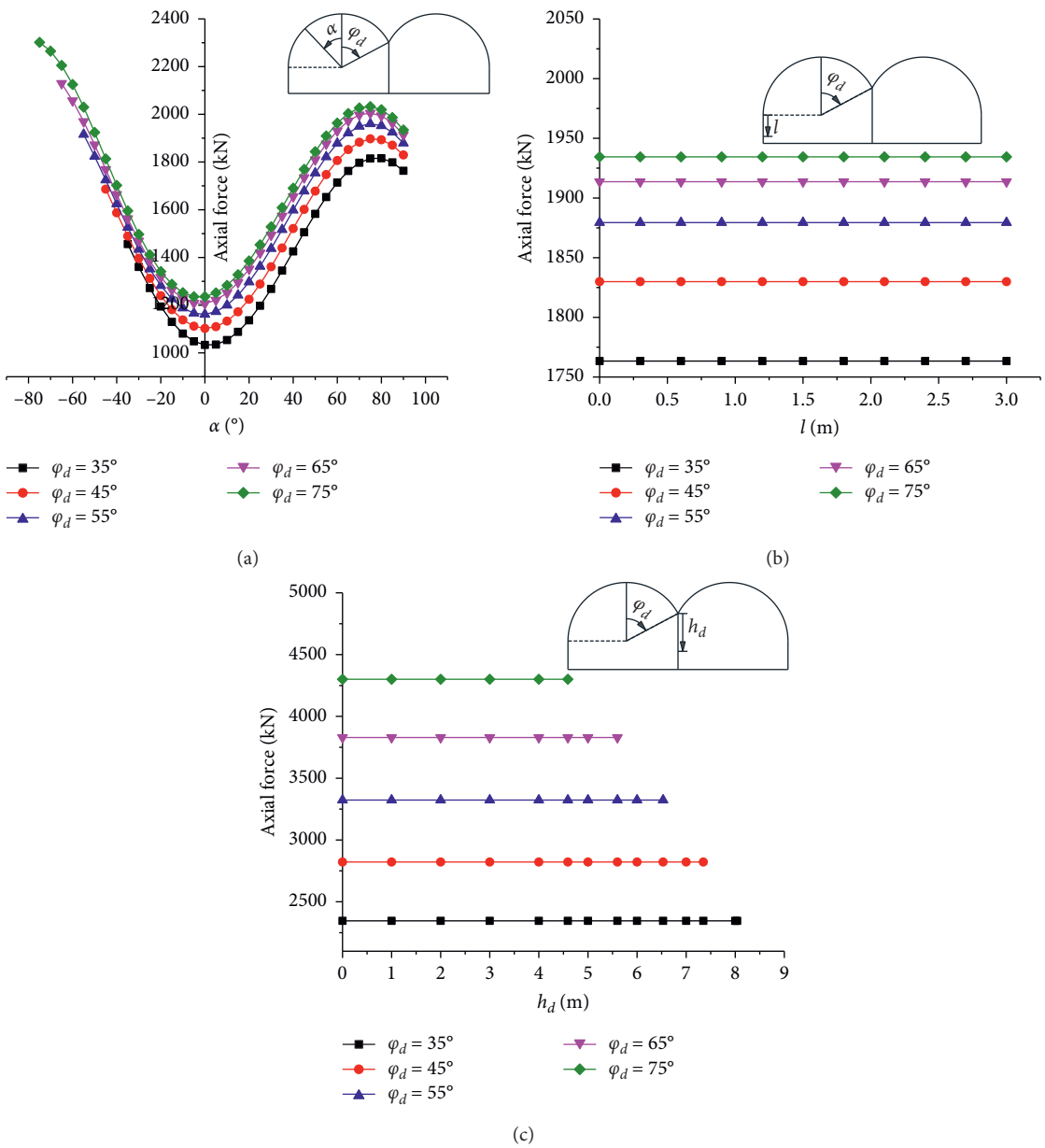

Figure 19: Variations of axial force with φ_d: (a) along the arch ring; (b) along the side wall, and (c) along the middle wall.

decreases as K increases for β in the range of 0° to about 120°, while as β becomes greater than 120°, the magnitude of shear force increases with increasing K. The magnitude of shear force along the side wall decreases in the top three tenths of the side wall and increases for the remaining section for which K increases in the range of 100–200 MPa/m. When K is greater than 500 MPa/m, the magnitude of shear force decreases with increasing K for the top one tenth and bottom four tenths and increases for the remaining section of side wall. Overall, the elastic resistance coefficient has more influence on the internal forces along the side wall. This may be because the elastic resistance is only applied to the side wall but is not present over the arch ring. The situation when elastic resistance is present over the entire lining ring needs further exploration in the future.

5.3. The Effect of Opening Angle. The opening angle φ_d is one of the main geometrical parameters determining the dimension of the double-arched tunnel, which is measured from the arch crown to the top of the middle wall as shown in Figure 2. The analysis of the opening angle serves as an important reference for designing and optimizing the cross section of the double-arched tunnel.

The arch ring radius R is assumed to be a constant. In such a case, the tunnel width B and height of middle wall h_d would change in accordance with the change of φ_d. The adopted values in the analysis are shown in Table 5. The results of the internal forces obtained for different cases are shown in Figures 18–20.

It can be found that for both side walls and middle wall, the bending moment and axial force increase as φ_d increases.

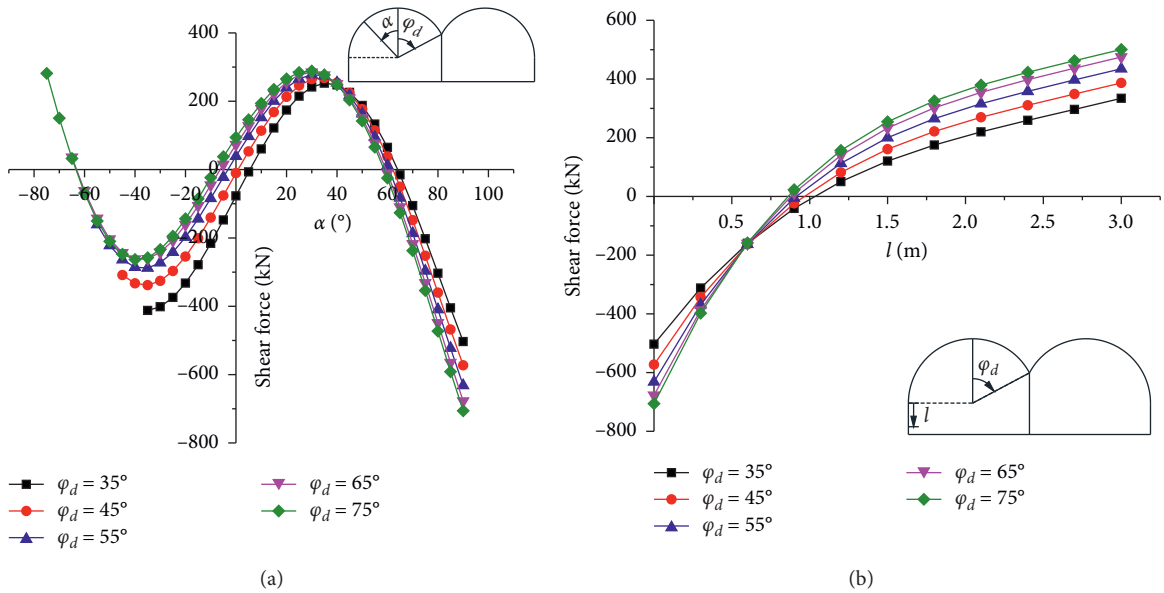

Figure 20: Variations of shear force with φ_d: (a) along the arch ring; (b) along the side wall.

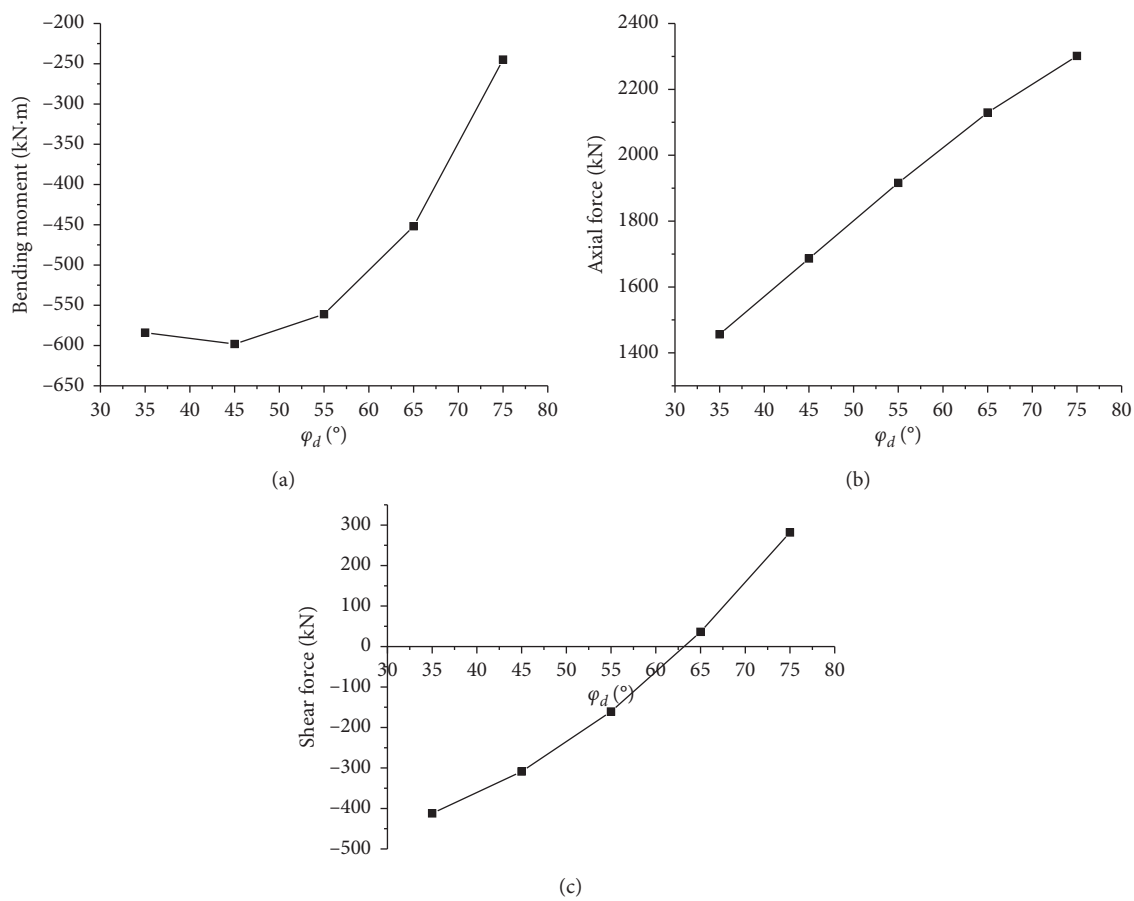

Figure 21: Variations of internal forces at the contact interface between the arch ring and the top of the middle wall with φ_d: (a) bending moment; (b) axial force; (c) shear force.

The magnitude of shear force of the side wall also increases with increasing φ_d except in the range about $l = 0.6$–1.0 m. The axial force of the arch ring also increases with the increase in opening angle. The variation of bending moment and shear force of the arch ring with φ_d is more complex. A greater change in the internal forces happens near the

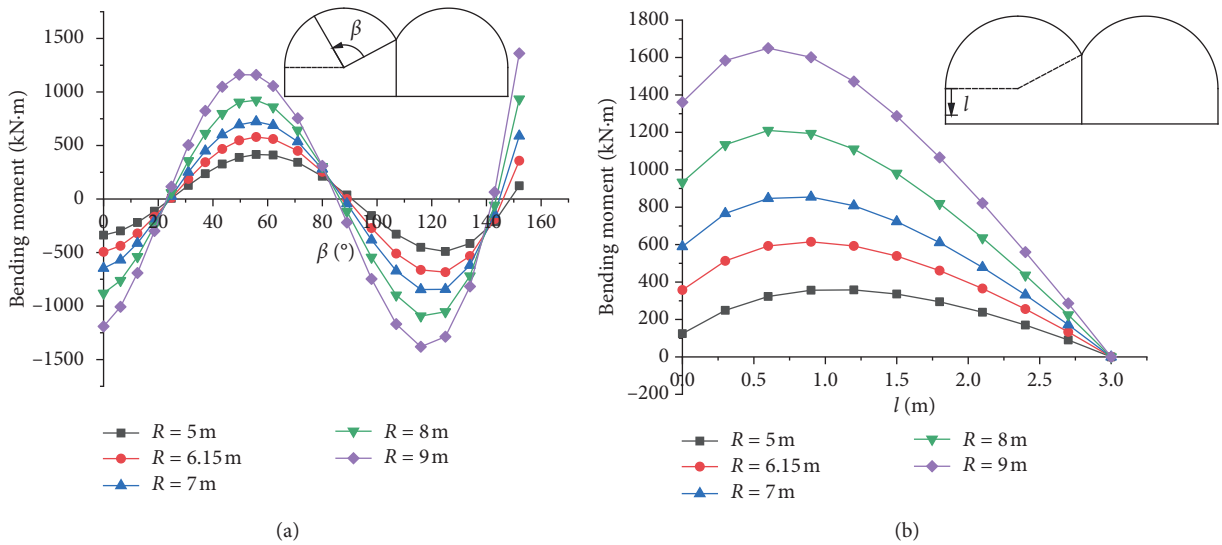

Figure 22: Variations of bending moment with R: (a) along the arch ring; (b) along the side wall.

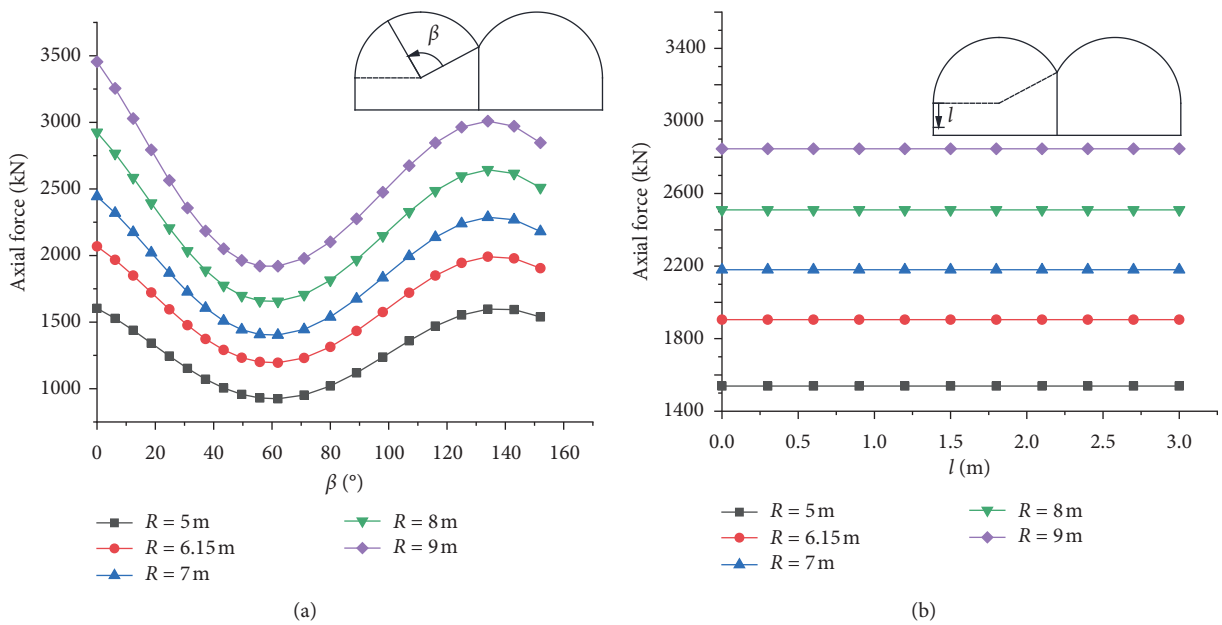

Figure 23: Continued.

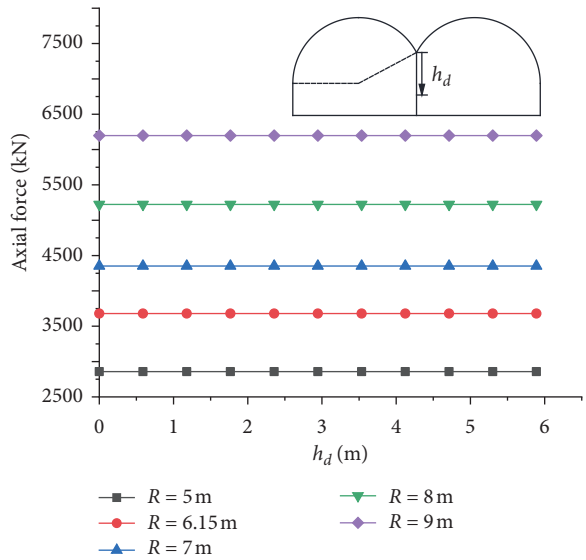

(c)

Figure 23: Variations of axial force with R: (a) along the arch ring; (b) along the side wall; (c) along the middle wall.

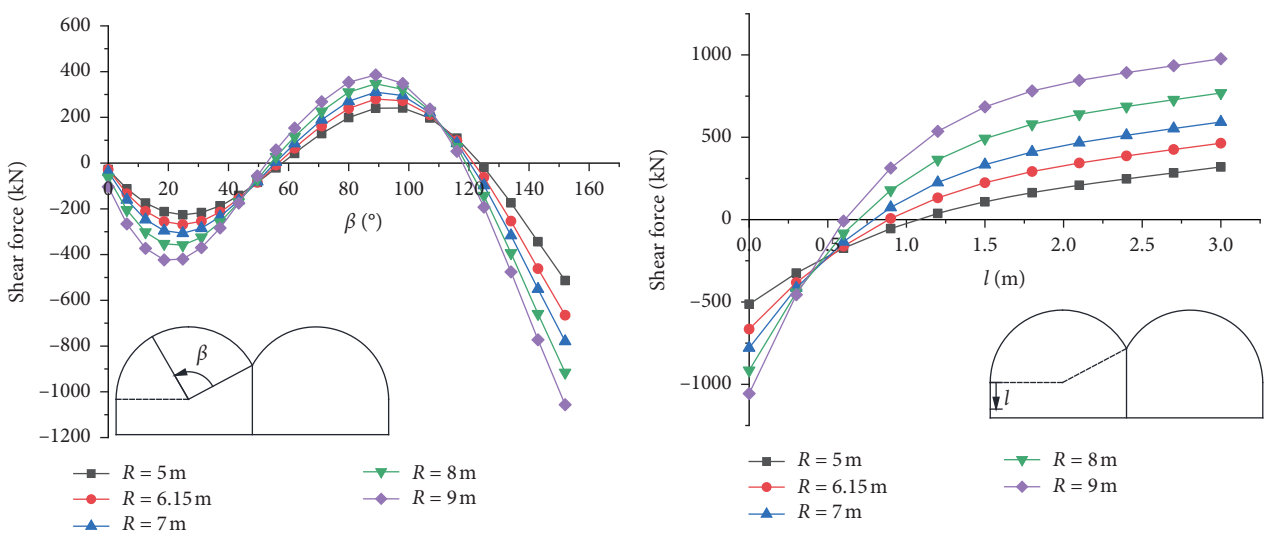

(a) (b)

Figure 24: Variations of shear force with R: (a) along the arch ring; (b) along the side wall.

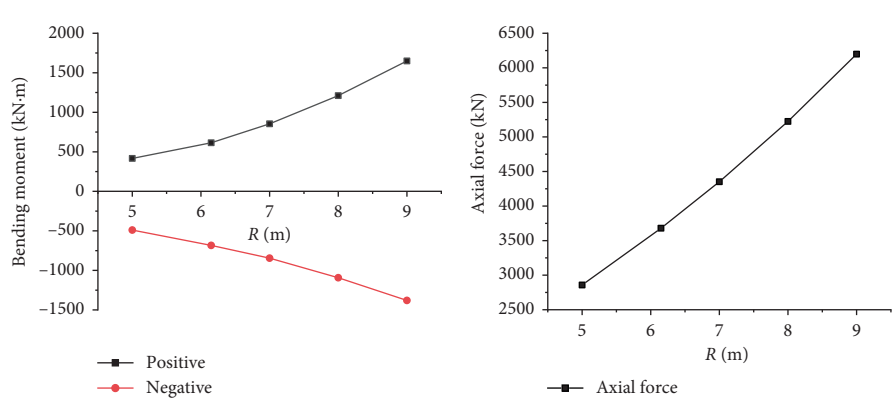

(a) (b)

Figure 25: Continued.

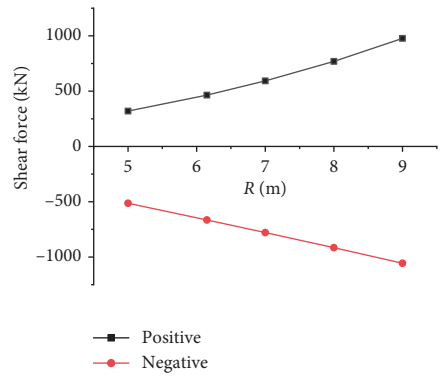

(c)

Figure 25: Variations of largest magnitudes of internal forces with R: (a) bending moment; (b) axial force; (c) shear forcel.

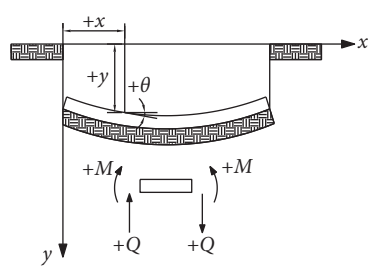

Figure 26: Schematic diagram of elastic foundation beam

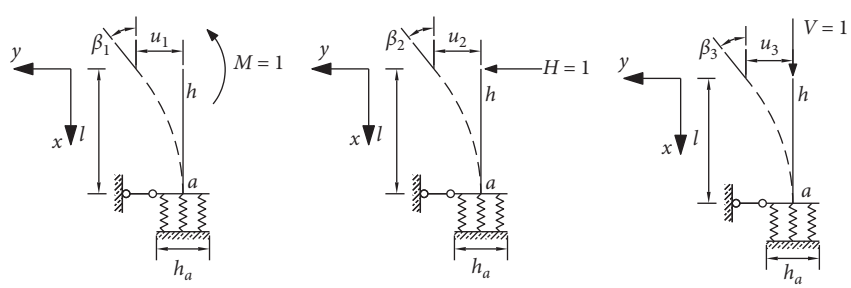

(a) (b) (c)

Figure 27: The displacements of the side wall under unit load: (a) $M = 1$; (b) $H = 1$; (c) $V = 1$.

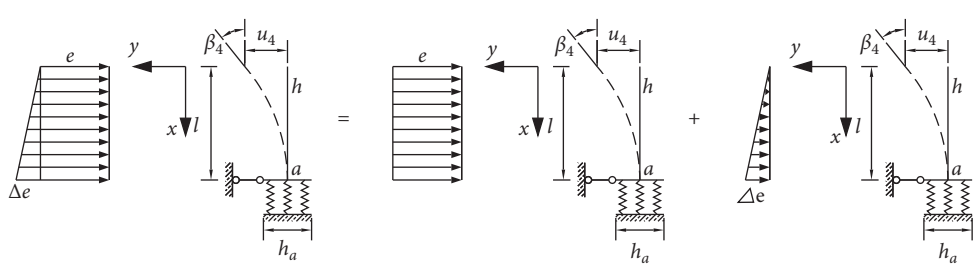

Figure 28: The displacement of the side wall under lateral trapezoidal pressure.

conjunction region between the arch ring and the top of the middle wall. Since the conjunction region between the arch ring and the top of middle wall is a special location closely related to φ_d where faults may exist and seepage may usually take place [40], it is of key concern for construction and design. Therefore, the influence of φ_d on the internal force at this location is explored in more details. Figure 21 shows the variation of the internal forces at the conjunction region

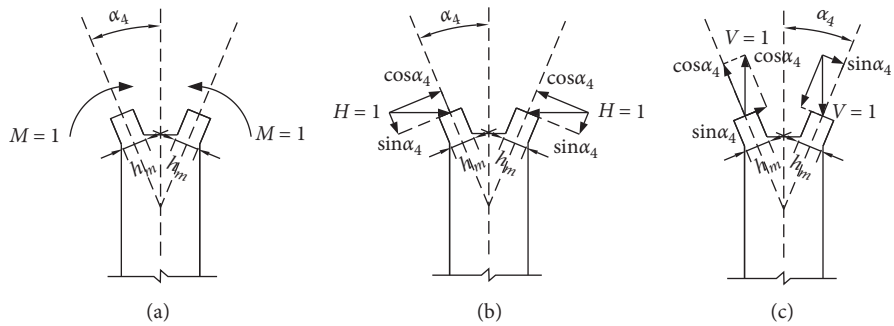

Figure 29: The schematic diagram of the top of the middle wall under the unit load: (a) $M = 1$; (b) $H = 1$; (c) $V = 1$.

between the arch ring and the top of the middle wall under different φ_d. As can be seen from Figure 21, in the range of opening angles considered, the bending moment increases initially to about 630 kN m and then decreases as φ_d further increases. In contrast, the shear force decreases initially to zero and reverses direction as φ_d further increases. The axial force increases almost linearly with increasing φ_d. Besides, Figure 19(a) shows that when φ_d exceeds 55°, the axial force at the conjunction region will be the largest along the arch ring. Considering that the conjunction region is the most difficult part for construction and the quality of lining installation may be the lowest in comparison to other parts of the lining structure, it is practically safer to maintain the axial force at the conjunction region at a low level. Therefore, it is suggested that φ_d should not exceed 55°.

5.4. The effect of tunnel span. The tunnel span of double-arched tunnel is represented by the total width B and is mainly decided by the radius of arch ring R and thickness of middle wall. In order to analyse the effect of tunnel span on the internal forces, the height of the side wall and middle wall and the opening angle in Figure 8(a) are not changed, and the burial depth remains 9.5 m, while the outer radius of arch ring increases from 5 m to 9 m at an increment of 1 m, and the outer radius 6.15 m in Figure 8(a) is still maintained. Neglecting the thickness of the middle wall in the analysis, the total width of the double-arched tunnel increases from 18.83 m to 33.89 m accordingly. The results of the internal forces obtained for different cases are shown in Figures 22–24.

A larger tunnel span means a larger area of tunnel lining subjected to the vertical pressure on the top of the tunnel. Figures 22–24 show that the variation trends of the internal forces with tunnel span are very similar to those with burial depth as shown in the Figures 11–13. As R increases, the absolute magnitude of axial force increases, while most of the absolute magnitude of the bending moment and shear force also increase except that near the inflection point. The point of the largest positive bending moment and the zero point of shear force of side wall move towards the top of side wall from about 1.2 m to 0.6 m as R increases. The largest negative bending moment is present in the arch ring at locations of $\beta = 125°$ to $\beta = 116°$ as R increases. These positions are different from those in the analysis of burial depth H.

The largest positive of bending moment is present in the side wall about $I = 0.6$ m to $I = 1.2$ m except that at R = 5 m, the largest positive of bending moment is located in the arch ring at location about $\beta = 56°$. The maximum axial force is in the middle wall as shown in Figure 23. The largest shear force occurs at the bottom and top of the side wall as shown in Figure 24. As shown in Figure 25, nonlinear correlations between the largest internal forces and R are observed, which are different from the linear correlations as between the largest internal forces and burial depth. This indicates that the tunnel span is more influential to the internal forces than the burial depth (Figure 25).

6. Conclusions

This paper derived the analytical solutions for the internal forces of shallow double-arched tunnel based on the force method and elastic foundation beam model. The internal forces predicted by the proposed analytical solutions were in good agreement with the results of numerical simulations. The influences of different factors on the internal forces were investigated using the newly derived solutions. Based on the calculated and numerical simulation data, some conclusions are drawn as follows:

(1) The variation trend of the internal forces in different burial depths is similar, but the absolute values increase as the burial depth increases.

(2) The elastic resistance coefficient of the surrounding rock has a notable effect on the internal force of the side wall. In general, the internal forces decrease with increasing elastic resistance coefficient, which indicates a better performance of lining structure surrounded by rock masses with higher quality.

(3) The internal forces of the lining structure can be significantly affected by the opening angle of the double-arched tunnel, especially at the conjunction region between the arch ring and the top of the middle wall. Considering the reduced construction quality at the conjunction region, it is recommended that the open angle should lie in the range of 35°–55° for the safety of the lining structure.

(4) Overall, the internal forces increase with increasing tunnel span. The correlations between the largest internal forces with tunnel span are nonlinear

(5) The results of the internal forces along the lining structure mainly show that the intrados of the crown and extrados of the haunch of the arch ring experience the largest tensile forces, while the side and middle walls experience larger compressive forces than other regions. These zones require special attention during the construction and design.

The derived analytical solutions provide fast estimations for the internal forces and deformation of double-arched lining structures, which does not rely on either costly comprehensive field monitoring or time-consuming sophisticated numerical modelling. However, it should be noted that both the analytical solutions and numerical simulations conducted in this paper are based on the load-structure method but do not consider the dynamic interaction between tunnel structure and surrounding rock masses. Furthermore, it is likely that the double-arched tunnels will lie in the sloping region which induces unsymmetrical pressures. Both deserve further investigations in the future.

Appendix

A. The Coefficients on the Top of Side Wall

The displacement coefficients at the conjunction region between the arch ring and the side wall can be obtained by solving the top coefficients of the side wall using the elastic foundation method. During the derivation of the displacement coefficients, the directions of the force and displacement are in accordance with the elastic foundation method, which are shown in Figure 26. After the displacement coefficients have been obtained, the direction of the displacement is changed to the specified direction in the derivation of the analytical solutions, in which the angular displacement is positive when the turning direction is outwards and the horizontal displacement is positive with outward movement.

The equation set for the elastic foundation beam in Figure 26 is as follows:

$$\left.\begin{aligned} y &= y_0\varphi_1 + \theta_0\frac{1}{2a}\varphi_2 - M_0\frac{2a^2}{bK}\varphi_3 - Q_0\frac{a}{bK}\varphi_4 \\ \theta &= -y_0 a\varphi_4 + \theta_0\varphi_1 - M_0\frac{2a^3}{bK}\varphi_2 - Q_0\frac{2a^2}{bK}\varphi_3 \\ M &= y_0\frac{bK}{2a^2}\varphi_3 + \theta_0\frac{bK}{4a^3}\varphi_4 + M_0\varphi_1 + Q_0\frac{1}{2a}\varphi_2 \\ Q &= y_0\frac{bK}{2a}\varphi_2 + \theta_0\frac{bK}{2a^2}\varphi_3 - M_0 a\varphi_4 + Q_0\varphi_1 \end{aligned}\right\}, \quad (A.1)$$

where y_0, θ_0, M_0, and Q_0 are the initial parameters at the initial cross section of the elastic foundation beam; $a = \sqrt[4]{((Kb)/(E'I))}$, of which K is the elastic resistance coefficient, b is the width along the longitudinal direction and $b = 1$ is adopted in the calculation of the current study; and $\varphi_1 \sim \varphi_4$ are given by $\varphi_1 = \text{chax}\cos ax$, $\varphi_2 = \text{chax}\sin ax + \text{shax}\cos ax$, $\varphi_3 = \text{shax}\sin ax$, and $\varphi_4 = \text{chax}\sin ax - \text{shax}\cos ax$.

A.1. The Coefficients under the Unit Load. Taking the left side wall as an example, the displacements occurring at the top of the side wall under the unit load are shown in Figure 27.

As for $M = 1$ shown in Figure 27(a), the initial parameters are as follows:

$$\begin{cases} x = 0\text{: } M = 1\left(M_0 = -1\right), \\ Q = 0\left(Q_0 = 0\right) \\ x = l\text{: } y = 0, \\ \theta = \dfrac{M|_{x=l}}{k_a I_a}, \end{cases} \quad (A.2)$$

where k_a is the elastic resistance coefficient at the bottom of the side wall, which is equal to K, and I_a is the polar moment of inertia of the bottom of the side wall with respect to the longitudinal direction, which equals to I in the current study.

Substituting equation (A.2) into equation (A.1) yields the angular and horizontal displacements by turning the directions of both to the specified direction as mentioned previously. Furthermore, under the assumption that the tunnel experiences uniform pressure in the vertical direction and the frictional force on the side wall is large enough, the vertical displacement can be set to 0. Thus, the displacement coefficients at the conjunction region between the arch ring and the top of the left side wall are as follows:

$$\left.\begin{aligned} \theta_0 = \beta_1 = \beta_{1l} &= \frac{4a^3}{bK}\frac{\left[\varphi_{11}(l) + A\varphi_{12}(l)\right]}{\left[\varphi_9(l) + A\varphi_{10}(l)\right]} \\ y_0 = u_1 = u_{1l} &= \frac{2a^2}{bK}\frac{\left[\varphi_{13}(l) + A\varphi_{11}(l)\right]}{\left[\varphi_9(l) + A\varphi_{10}(l)\right]} \\ v_{1l} &= 0 \end{aligned}\right\}. \quad (A.3)$$

Substituting the obtained y_0 and θ_0 back into equation (A.1), the internal forces of the side wall under $M = 1$ are as follows:

$$\left.\begin{aligned} M_{M=1} &= -\frac{\varphi_{13}(l) + A\varphi_{11}(l)}{\varphi_9(l) + A\varphi_{10}(l)}\varphi_3 + \frac{\varphi_{11}(l) + A\varphi_{12}(l)}{\varphi_9(l) + A\varphi_{10}(l)}\varphi_4 + \varphi_1 \\ Q_{M=1} &= a\frac{\varphi_{13}(l) + A\varphi_{11}(l)}{\varphi_9(l) + A\varphi_{10}(l)}\varphi_2 - 2a\frac{\varphi_{11}(l) + A\varphi_{12}(l)}{\varphi_9(l) + A\varphi_{10}(l)}\varphi_3 + a\varphi_4 \end{aligned}\right\}, \quad (A.4)$$

where $A = ((bK)/(2a^3 k_a I_a))$, $\varphi_9(x) = (1/2)(ch^2 ax + \cos^2 ax)$, $\varphi_{10}(x) = (1/2)(chaxshax - \sin ax\cos ax)$, $\varphi_{11}(x) = (1/2)(shaxchax + \sin ax\cos ax)$, $\varphi_{12}(x) = (1/2)(ch^2 ax - \sin^2 ax)$, and $\varphi_{13}(x) = (1/2)(sh^2 ax + \sin^2 ax)$.

By using the same method, the initial parameters under $H = 1$ and $V = 1$ conditions are presented in the following equations:

$$\begin{cases} x = 0\colon\ M = 0\left(M_0 = 0\right), \\ H = 1\left(Q_0 = -1\right), \\ x = l\colon\ y = 0, \\ \theta = \dfrac{M|_{x=l}}{k_a I_a}, \end{cases} \tag{A.5}$$

$$\begin{cases} x = 0\colon\ M = 0\left(M_0 = 0\right), \\ Q = 0\left(Q_0 = 0\right), \\ x = l\colon\ y = 0, \\ \theta = \dfrac{M|_{x=l}}{k_a I_a} - \dfrac{e_0}{k_a I_a}, \end{cases} \tag{A.6}$$

where e_0 is the eccentricity between the center line of the side wall and the center line of the bottom of the side wall, which equals to 0 in the calculation of the analytical solutions in the current study.

The displacement coefficients for $H = 1$ and $V = 1$ are as follows:

$$\begin{aligned} &\left.\begin{aligned} \theta_0 = \beta_2 = \beta_{2l} &= \frac{2a^2}{bK}\frac{\varphi_{13}(l) + A\varphi_{11}(l)}{\varphi_9(l) + A\varphi_{10}(l)} \\ y_0 = u_2 = u_{2l} &= \frac{2a}{bK}\frac{\varphi_{10}(l) + A\varphi_{13}(l)}{\varphi_9(l) + A\varphi_{10}(l)} \\ v_{2l} &= 0 \end{aligned}\right\}, \\ &\left.\begin{aligned} \theta_0 = \beta_3 = \beta_{3l} &= \frac{e_0}{k_a I_a}\frac{\varphi_1(l)}{\varphi_9(l) + A\varphi_{10}(l)} \\ y_0 = u_3 = u_{3l} &= \frac{e_0}{2ak_a I_a}\frac{\varphi_2(l)}{\varphi_9(l) + A\varphi_{10}(l)} \\ v_{3l} &= 0 \end{aligned}\right\}. \end{aligned} \tag{A.7}$$

The internal forces of the side wall for $H = 1$ and $V = 1$ are as follows:

$$\begin{aligned} &\left.\begin{aligned} M_{H=1} &= -\frac{\varphi_{10}(l) + A\varphi_{13}(l)}{\varphi_9(l) + A\varphi_{10}(l)}\frac{1}{a}\varphi_3 + \frac{\varphi_{13}(l) + A\varphi_{11}(l)}{\varphi_9(l) + A\varphi_{10}(l)}\frac{1}{2a}\varphi_4 + \frac{1}{2a}\varphi_2 \\ Q_{H=1} &= \frac{\varphi_{10}(l) + A\varphi_{13}(l)}{\varphi_9(l) + A\varphi_{10}(l)}\varphi_2 - \frac{\varphi_{13}(l) + A\varphi_{11}(l)}{\varphi_9(l) + A\varphi_{10}(l)}\varphi_3 - \varphi_1 \end{aligned}\right\}, \\ &\left.\begin{aligned} M_{V=1} &= -\frac{e_0 bK}{4a^3 k_a I_a}\frac{\varphi_2(l)\varphi_3}{\varphi_9 + A\varphi_{10}} + \frac{e_0 bK}{4a^3 k_a I_a}\frac{\varphi_1(l)\varphi_4}{\varphi_9 + A\varphi_{10}} \\ Q_{V=1} &= \frac{e_0 bK}{4a^2 k_a I_a}\frac{\varphi_2(l)\varphi_2}{\varphi_9 + A\varphi_{10}} - \frac{e_0 bK}{2a^2 k_a I_a}\frac{\varphi_1(l)\varphi_3}{\varphi_9 + A\varphi_{10}} \end{aligned}\right\}. \end{aligned} \tag{A.8}$$

A.2. The Coefficients under the Lateral Trapezoidal Pressure. The lateral trapezoidal pressure $e + \Delta e$ exerted on the side wall can be considered as a uniform pressure $e = e_1 + f_1 \tan\alpha_1$ and a triangular pressure $\Delta e = l \cdot \tan\alpha_1$, which is shown in Figure 28.

According to the elastic foundation method, the equation set for the elastic foundation beam under the uniform pressure shown in Figure 28 is as follows:

$$\left.\begin{aligned}
y &= y_0\varphi_1 + \theta_0\frac{1}{2a}\varphi_2 - M_0\frac{2a^2}{bK}\varphi_3 - Q_0\frac{a}{bK}\varphi_4 - \frac{e}{bK}(1-\varphi_1)\\
\theta &= -y_0 a\varphi_4 + \theta_0\varphi_1 - M_0\frac{2a^3}{bK}\varphi_2 - Q_0\frac{2a^2}{bK}\varphi_3 - \frac{ae}{bK}\varphi_4\\
M &= y_0\frac{bK}{2a^2}\varphi_3 + \theta_0\frac{bK}{4a^3}\varphi_4 + M_0\varphi_1 + Q_0\frac{1}{2a}\varphi_2 + \frac{e}{2a^2}\varphi_3\\
Q &= y_0\frac{bK}{2a}\varphi_2 + \theta_0\frac{bK}{2a^2}\varphi_3 - M_0 a\varphi_4 + Q_0\varphi_1 + \frac{e}{2a}\varphi_2
\end{aligned}\right\}. \tag{A.9}$$

As for the pressure shown in Figure 28, the initial parameters are as follows:

$$\begin{cases}
x = 0\colon\ M = 0\,(M_0 = 0),\\
Q = 0\,(Q_0 = 0),\\
x = l\colon\ y = 0,\\
\theta = \dfrac{M|_{x=l}}{k_a I_a}.
\end{cases} \tag{A.10}$$

Substituting equation (A.10) into equation (A.9) and using the same method as in Section A.1, the displacement coefficients under the uniform pressure are as follows:

$$\left.\begin{aligned}
\theta_0 = \beta_e &= -\frac{a}{bK}\,\frac{\varphi_4(l) + A\varphi_3(l)}{\varphi_9(l) + A\varphi_{10}(l)}e\\
y_0 = u_e &= -\frac{1}{bK}\,\frac{\varphi_{14}(l) + A\varphi_{15}(l)}{\varphi_9(l) + A\varphi_{10}(l)}e
\end{aligned}\right\}, \tag{A.11}$$

where $\varphi_{14}(x) = (1/2)(ch^2 ax - \cos ax)^2$ and $\varphi_{15}(x) = (1/2)(shax + \sin ax)(chax - \cos ax)$.

The internal forces of the side wall under the uniform pressure are as follows:

$$\left.\begin{aligned}
M_e &= \frac{e}{2a^2}\,\frac{\varphi_{14}(l) + A\varphi_{15}(l)}{\varphi_9(l) + A\cdot\varphi_{10}(l)}\varphi_3 - \frac{e}{4a^2}\,\frac{\varphi_4(l) + A\varphi_3(l)}{\varphi_9(l) + A\varphi_{10}(l)}\varphi_4 - \frac{e}{2a^2}\varphi_3\\
Q_e &= -\frac{e}{2a}\,\frac{\varphi_{14}(l) + A\varphi_{15}(l)}{\varphi_9(l) + A\cdot\varphi_{10}(l)}\varphi_2 + \frac{e}{2a}\,\frac{\varphi_4(l) + A\varphi_3(l)}{\varphi_9(l) + A\varphi_{10}(l)}\varphi_3 + \frac{e}{2a}\varphi_2
\end{aligned}\right\}. \tag{A.12}$$

For the lateral triangular pressure $\Delta e = l\cdot\tan\alpha_1$, the equation set for the elastic foundation beam changes to the following:

$$\left.\begin{aligned}
y &= y_0\varphi_1 + \theta_0\frac{1}{2a}\varphi_2 - M_0\frac{2a^2}{bK}\varphi_3 - Q_0\frac{a}{bK}\varphi_4 - \frac{\Delta e}{bKl}\left(x - \frac{1}{2a}\varphi_2\right)\\
\theta &= -y_0 a\varphi_4 + \theta_0\varphi_1 - M_0\frac{2a^3}{bK}\varphi_2 - Q_0\frac{2a^2}{bK}\varphi_3 - \frac{\Delta e}{bKl}(1-\varphi_1)\\
M &= y_0\frac{bK}{2a^2}\varphi_3 + \theta_0\frac{bK}{4a^3}\varphi_4 + M_0\varphi_1 + Q_0\frac{1}{2a}\varphi_2 + \frac{\Delta e}{4a^3 l}\varphi_4\\
Q &= y_0\frac{bK}{2a}\varphi_2 + \theta_0\frac{bK}{2a^2}\varphi_3 - M_0 a\varphi_4 + Q_0\varphi_1 + \frac{\Delta e}{2a^2 l}\varphi_3
\end{aligned}\right\}. \tag{A.13}$$

The initial parameters are the same as in equation (A.10), and then the displacement coefficients can be derived as follows:

$$\left.\begin{aligned}\theta_0 = \beta_{\Delta e} &= -\frac{a}{bK}\frac{\varphi_4(l) - (\varphi_{14}(l)/al) + A[\varphi_3(l) - (\varphi_{10}(l)/al)]}{\varphi_9(l) + A\varphi_{10}(l)}\Delta e \\ y_0 = u_{\Delta e} &= -\frac{1}{bK}\frac{(\varphi_2(l)/2la) - \varphi_1(l) + A(\varphi_4(l)/2)}{\varphi_9(l) + A\cdot\varphi_{10}(l)}\Delta e\end{aligned}\right\}. \tag{A.14}$$

The internal forces of the side wall under the triangular pressure are as follows:

$$\left.\begin{aligned}M_{\Delta e} &= \frac{1}{2a^2}\frac{(\varphi_2(l)/2la) - \varphi_1(l) + A(\varphi_4(l)/2)}{\varphi_9(l) + A\varphi_{10}(l)}\Delta e\varphi_3 - \frac{1}{4a^2}\frac{\varphi_4(l) - (\varphi_{14}(l)/al) + A[\varphi_3(l) - (\varphi_{10}(l)/al)]}{\varphi_9(l) + A\varphi_{10}(l)}\Delta e\varphi_4 - \frac{\Delta e}{4a^3 l}\varphi_4 \\ Q_{\Delta e} &= -\frac{1}{2a}\frac{(\varphi_2(l)/2la) - \varphi_1(l) + A(\varphi_4(l)/2)}{\varphi_9(l) + A\varphi_{10}(l)}\Delta e\varphi_2 + \frac{1}{2a}\frac{\varphi_4(l) - (\varphi_{14}(l)/al) + A[\varphi_3(l) - (\varphi_{10}(l)/al)]}{\varphi_9(l) + A\varphi_{10}(l)}\Delta e\varphi_3 + \frac{\Delta e}{2a^2 l}\varphi_3\end{aligned}\right\}. \tag{A.15}$$

The total displacement coefficients of the side wall under the lateral trapezoidal pressure are as follows:

$$\left.\begin{aligned}\beta_{4l} = \beta_4 &= -\frac{a}{bK}\frac{\varphi_4(l) + A\varphi_3(l)}{\varphi_9(l) + A\varphi_{10}(l)}e - \frac{a}{bK}\frac{\varphi_4(l) - (\varphi_{14}(l)/al) + A[\varphi_3(l) - (\varphi_{10}(l)/al)]}{\varphi_9(l) + A\varphi_{10}(l)}\Delta e \\ u_{4l} = u_4 &= -\frac{1}{bK}\frac{\varphi_{14}(l) + A\varphi_{15}(l)}{\varphi_9(l) + A\varphi_{10}(l)}e - \frac{1}{bK}\frac{(\varphi_2(l)/2la) - \varphi_1(l) + A(\varphi_4(l)/2)}{\varphi_9(l) + A\cdot\varphi_{10}(l)}\Delta e\end{aligned}\right\}. \tag{A.16}$$

Accordingly, the coefficients for the right-side wall can be obtained utilizing the same method.

B. The Coefficients at the Top of Middle Wall

The schematic diagram of the top of the middle wall under the unit load $X_i = 1$ is shown in Figure 29. According to the decomposition of forces in Figure 29, the coefficients of the middle wall can be calculated separately.

Taking the left tunnel as an example, as for $M = 1$, the displacement coefficients at the top of the middle wall are as follows:

$$\left.\begin{aligned}\beta_{1r} &= \beta_1 = \frac{1}{k_d I_d} \\ u_{1r} &= u_1 = 0 \\ v_{1r} &= v_1 = 0\end{aligned}\right\}. \tag{B.1}$$

As for $H = 1$, the displacement coefficients are as follows:

$$\left.\begin{aligned}\beta_{2r} &= 0 \\ u_{2r} &= \frac{\sin^2\alpha_4}{k_d h_m} \\ v_{2r} &= -\frac{\cos\alpha_4\cdot\sin\alpha_4}{k_d h_m}\end{aligned}\right\}. \tag{B.2}$$

As for $V = 1$, the displacement coefficients are as follows:

$$\left.\begin{aligned}\beta_{3r} &= 0 \\ u_{3r} &= -\frac{\cos\alpha_4\cdot\sin\alpha_4}{k_d h_m} \\ v_{3r} &= \frac{\cos^2\alpha_4}{k_d h_m}\end{aligned}\right\}, \tag{B.3}$$

where k_d is the elastic resistance coefficient between the top of the middle wall and the arch ring, which is equal to the

elastic modulus E' of the lining structure in the analytical solutions, and I_d is the polar moment of inertia of the conjunction region between the arch ring and the top of the middle wall, which equals to I.

Accordingly, the coefficients for the right tunnel at the top of the middle wall can be obtained by utilizing the same method.

All the unknown coefficients in the derivation of the analytical solutions have been presented in Appendix A and B taking the left tunnel as an example. Other unknown coefficients in the derivation can be calculated using the basic coefficients and through the force analysis, which are not discussed for simplicity.

Abbreviations

A: Area of the cross section of arch ring
a: Bottom point of the side wall in the left tunnel
B: Total width of the double-arched tunnel
b: Width of side wall along the longitudinal direction
d: Foot of right arch of left tunnel on the top of middle wall
E: Elastic modulus of surrounding rock
E': Elastic modulus of lining structure
$e = e_1$: Lateral uniform pressure outside of double-arched tunnel
e_1': Lateral uniform pressure on the top of middle wall
f_1: Height of left half arch ring of left tunnel
f_2: Height of right half arch ring of left tunnel
G: Shear modulus of lining structure
H: Burial depth at the crown of the double-arched tunnel
H_1: Height from the top of middle wall to the ground surface
H_2: Height of the double-arched tunnel
H_p: The cut-off altitude separating deep tunnel from shallow tunnel
h: Foot of left arch of left tunnel on the top of side wall
h_a: Bottom width of left side wall
h_d: Height of middle wall
h_p: The load equivalent height
I: Polar moment of inertia of the arch ring's cross section with respect to the longitudinal direction
I_a: Polar moment of inertia of the bottom of the side wall with respect to the longitudinal direction
I_d: Polar moment of inertia of the conjunction region between the arch ring and the top of the middle wall
K: Elastic resistance coefficient of surrounding rock
k: The nonuniform coefficient of the shear stress, which is taken to be 1.2 for the rectangular cross-section
k_a: Elastic resistance coefficient at the bottom of the side wall
k_d: Elastic resistance coefficient between the top of the middle wall and the arch ring
l: Height of side wall of left tunnel
l_1: Width of left half arch ring of left tunnel
l_2: Width of right half arch ring of left tunnel
M_{ip}^o: Bending moment of arch ring under the active pressures
$M_{\Delta e}$: Bending moment of side wall induced by the triangular pressure exerted on the side wall along the vertical direction
M_0: Initial bending moment at the initial cross section of the elastic foundation beam
M_e: Bending moment of side wall induced by the uniform pressure exerted on the side wall along the vertical direction
$M_{H=1}$: Bending moment of side wall induced by the unit horizontal force exerted on the top of side wall
$M_i\,(M_j)$: Bending moments of arch ring under the unit loads $X_i(X_j) = 1$
M_{ia}: Bending moment of arch ring
M_{im}: Bending moment of middle wall
M_{is}: Bending moment of side wall
$M_{M=1}$: Bending moment of side wall induced by the unit bending moment exerted on the top of side wall
$M_{V=1}$: Bending moment of side wall induced by the unit vertical force exerted on the top of sidewall
N_{ip}^o: Axial force of arch ring under the active pressures
$N_i\,(N_j)$: Axial forces of arch ring under the unit loads $X_i\,(X_j) = 1$
N_{ia}: Axial force of arch ring
N_{im}: Axial force of middle wall
N_{is}: Axial force of side wall
Q_{ip}^o: Shear force of arch ring under the active pressures
$Q_{\Delta e}$: Shear force of side wall induced by the triangular pressure exerted on the side wall along the vertical direction
Q_0: Initial shear force at the initial cross section of the elastic foundation beam
Q_e: Shear force of side wall induced by the uniform pressure exerted on the side wall along the vertical direction
$Q_{H=1}$: Shear force of side wall induced by the unit horizontal force exerted on the top of side wall
$Q_i\,(Q_j)$: Shear forces of arch ring under the unit loads $X_i\,(X_j) = 1$
Q_{ia}: Shear force of arch ring

Q_{im}: Shear force of middle wall
Q_{is}: Shear force of side wall
$Q_{M=1}$: Shear force of side wall induced by the unit bending moment exerted on the top of side wall
$Q_{v=1}$: Shear force of side wall induced by the unit vertical force exerted on the top of side wall
q: Vertical uniform pressure on the top of tunnel
q': Vertical triangular pressure on the top of middle wall
R: Outer radius of the arch ring of left tunnel
s: Arch length
u^o_{pl}: Horizontal displacement of the left arch foot under the active pressures
u^o_{pr}: Horizontal displacement of the right arch foot under the active pressures.
u_{il}: Horizontal displacement of the left arch foot under the unit loads $X_i = 1$
u_{ir}: Horizontal displacement of the right arch foot under the unit loads $X_i = 1$
u_{pl}: Horizontal displacement of the left arch foot of left tunnel
u_{pr}: Horizontal displacement of the right arch foot of left tunnel
v^o_{pl}: Vertical displacement of the left arch foot under the active pressures
v^o_{pr}: Vertical displacement of the right arch foot under the active pressures
v_{il}: Vertical displacement of the left arch foot under the unit loads $X_i = 1$
v_{ir}: Vertical displacement of the right arch foot under the unit loads $X_i = 1$
v_{pl}: Vertical displacement of the left arch foot of left tunnel
v_{pr}: Vertical displacement of the right arch foot of left tunnel
X_{ip}: The redundant internal forces of the crown section of the arch ring
y_0: Initial vertical displacement at the initial cross section of the elastic foundation beam
α_1: The growth angle of lateral earth pressure outside of double-arched tunnel
α_2: The growth angle of lateral earth pressure on the top of middle wall
α_3: The growth angle of vertical earth pressure on the top of middle wall
β: Angle between the failure surfaces and the horizontal for both sides of the tunnel
β^o_{pl}: Angular displacement of the left arch foot under the active pressures
β^o_{pr}: Angular displacement of the right arch foot under the active pressures
β_{il}: Angular displacement of the left arch foot under the unit loads $X_i = 1$
β_{ir}: Angular displacement of the right arch foot under the unit loads $X_i = 1$
β_{pl}: Angular displacement of the left arch foot of left tunnel
β_{pr}: Angular displacement of the right arch foot of left tunnel
δ_{ij}: Flexibility coefficients of the arch ring
$\Delta e = f_1 \tan \alpha_1$: Lateral triangular pressure outside of double-arched tunnel
$\Delta e = f_2 \tan \alpha_2$: Lateral triangular pressure on the top of middle wall
Δ_{ip}: Displacement induced by the active pressure in the direction of X_{ip} at the cross section of the tunnel crown
φ: The calculated friction angle of surrounding rock masses
φ_h: Angle between crown and left arch foot on the top of left side wall of left tunnel
φ_d: Angle between crown and right arch foot on the top of middle wall of left tunnel
γ: The unit weight of the surrounding rock mass
γ': Unit weight of lining structure
μ: Poisson's ratio of surrounding rock
μ': Poisson's ratio of lining structure
λ: The lateral pressure coefficient
θ: Friction angle of sliding surface
θ_0: Initial angle displacement at the initial cross section of the elastic foundation beam.

Data Availability

The data used to support the findings of this study are available from the corresponding author upon request.

Conflicts of Interest

The authors declare that they have no conflicts of interest.

Acknowledgments

The fruitful discussion with Dr. Shuaifeng Wang on the application and formulation of the force method is highly appreciated. This research was funded by the Powerchina Roadbridge Group Co., Ltd. (grant no. HHZ-JGY-FW-03) and the National Natural Science Foundation of China (grant no. 41672262).

References

[1] S. Wang, C. Li, Y. Wang et al., ""Evolution characteristics analysis of pressure-arch in a double-arch tunnel," *Tehnicki Vjesnik - Technical Gazette*, vol. 23, no. 1, pp. 181–189, 2016.
[2] Y. Luo, J. Chen, Z. Shi et al., "Mechanical and deformation characteristics and optimization of support parameters for superlarge-span tunnel: a case study from laohushan tunnel," *Advances In Civil Engineering*, vol. 2020, Article ID 8882019, 17 pages, 2020.
[3] S. Wang, C. Liu, G. Ma et al., "Experimental investigation on the influence of regional concrete spalling on shield tunnel segments," *Advances In Civil Engineering*, vol. 2019, Article ID 1829124, 15 pages, 2019.

[4] X. Jiang, F. Wang, H. Yang et al., "Parameter sensitivity of shallow-bias tunnel with a clear distance located in rock," *Advances In Civil Engineering*, vol. 2018, Article ID 5791354, 11 pages, 2018.

[5] H. Yang and X. Jiang, "Seismic response of tunnel lining for shallow-bias tunnel with a small clear distance under wenchuan earthquake," *Advances In Civil Engineering*, vol. 2018, Article ID 2578062, 10 pages, 2018.

[6] S. Hussain, Z. Ur Rehman, N. Mohammad et al., "Numerical modeling for engineering analysis and designing of optimum support systems for headrace tunnel," *Advances In Civil Engineering*, vol. 2018, Article ID 7159873, 10 pages, 2018.

[7] I. Kheyrandish, M. Ahmadi, and H. Jahankhah, "A numerical analysis of effect of segmental lining joints on tunnel support internal forces under seismic loading," *Journal of Mining and Environment*, vol. 10, no. 4, pp. 979–999, 2019.

[8] E. Bilotta and G. Russo, "Internal forces arising in the segmental lining of an earth pressure balance-bored tunnel," *Journal of Geotechnical and Geoenvironmental Engineering*, vol. 139, no. 10, pp. 1765–1780, 2013.

[9] J. Li, Y. Fang, C. Liu et al., "Performance investigation of tunnel lining with cavities around surrounding rocks," *Advances In Civil Engineering*, vol. 2020, Article ID 1364984, 5 pages, 2020.

[10] Q. Yan, C. Zhang, G. Lin et al., "Field monitoring of deformations and internal forces of surrounding rocks and lining structures in the construction of the gangkou double-arched tunnel—a case study," *Applied Sciences*, vol. 7, no. 2, Article ID 169, 2017.

[11] Y. Yuan, S. Wang, G. Du et al., "In-situ testing study of lining system of double-arched tunnel," *Chinese Journal of Rock Mechanics and Engineering*, vol. 24, no. 3, pp. 480–484, 2005.

[12] J. Lai, J. Qiu, H. Fan et al., "Structural safety assessment of existing multiarch tunnel: a case study," *Advances In Materials Science And Engineering*, vol. 2017, Article ID 1697041, 11 pages, 2017.

[13] J. Zhang, K. Sun, F. Lu et al., ""Model test study of surrounding rock pressure distribution and mechanical characteristics of unequal-span double-arch railway tunnel," *Rock and Soil Mechanics*, vol. 36, no. 11, pp. 3077–3084, 2015.

[14] J. He, C. Zhang, G. Yang et al., "Experimental study on mechanical behavior of nonsymmetric multi-arch tunnel in sand-cobble ground," *China Civil Engineering Journal*, vol. 50, no. 4, pp. 116–124, 2017.

[15] S. Li, C. Yuan, X. Feng, and S. Li, "Mechanical behaviour of a large-span double-arch tunnel," *KSCE Journal of Civil Engineering*, vol. 20, no. 7, pp. 2737–2745, 2016.

[16] F. Yu and L. Yang, "A study of arcade tunnel load and predigesting calculation," *Chinese Journal of Underground Space Engineering*, vol. 2, no. 5, pp. 770–774, 2006.

[17] Z. Zhang and C. He, "Study on mechanical behaviours of designing and construction for center pillar of double-arched tunnel," *Chinese Journal of Rock Mechanics and Engineering*, vol. 25, no. 8, pp. 1632–1638, 2006.

[18] X. Li and W. Zhang, "Stability analysis of surrounding rock of multi-arch tunnel based on coupled fluid-solid theorem," *Chinese Journal of Rock Mechanics and Engineering*, vol. 26, no. 5, pp. 1056–1064, 2007.

[19] Z. Mao, X. Wang, N. An, X. Li, and R. Wei, "Water disaster susceptible areas in loess multi-arch tunnel construction under the lateral recharge condition," *KSCE Journal of Civil Engineering*, vol. 23, no. 10, pp. 4564–4577, 2019.

[20] C. Liu, H. Yang, X. Jiang, and H. Shi, "Shaking table test and numerical simulation for acceleration response laws of shallow-buried biased double-arch tunnel," *Journal of Vibroengineering*, vol. 21, no. 4, pp. 1188–1200, 2019.

[21] B. Min, X. Zhang, C. Zhang et al., "Mechanical behavior of double-arch tunnels under the effect of voids on the top of the middle wall," *Symmetry*, vol. 10, no. 12, Article ID 703, 2018.

[22] X. Zhang, Z. Ye, B. Min et al., "Effect of voids behind lining on the failure behavior of symmetrical double-arch tunnels," *Symmetry*, vol. 11, no. 10, Article ID 1311, 2019.

[23] X. Hu, Z. Zhang, and L. Teng, "An analytical method for internal forces in DOT shield-driven tunnel," *Tunnelling and Underground Space Technology*, vol. 24, no. 6, pp. 675–688, 2009.

[24] O. P. M. Vitali, T. B. Celestino, and A. Bobet, "Analytical solution for tunnels not aligned with geostatic principal stress directions," *Tunnelling and Underground Space Technology*, vol. 82, pp. 394–405, 2018.

[25] M. Zhu, Y. Yang, F. Gao et al., "Analytical solution of tunnel surrounding rock for stress and displacement based on lade–duncan criterion," *Advances In Civil Engineering*, vol. 2018, Article ID 5363658, 7 pages, 2018.

[26] H. El Naggar and S. D. Hinchberger, "An analytical solution for jointed tunnel linings in elastic soil or rock," *Canadian Geotechnical Journal*, vol. 45, no. 11, pp. 1572–1593, 2008.

[27] K. M. Lee, X. Y. Hou, X. W. Ge, and Y. Tang, "An analytical solution for a jointed shield-driven tunnel lining," *International Journal for Numerical and Analytical Methods in Geomechanics*, vol. 25, no. 4, pp. 365–390, 2001.

[28] J. Wang, W. Huang, R. Xu, Z. Yang, and R. Xu, "Analytical approach for circular-jointed shield tunnel lining based on the state space method," *International Journal for Numerical and Analytical Methods in Geomechanics*, vol. 44, no. 5, pp. 575–595, 2020.

[29] J. C. Wang, W. M. Huang, R. Q. Xu et al., ""Analytical solution for segmental-tunnel lining incorporating interaction between adjacent rings," *Journal Of Engineering Mechanics*, vol. 146, no. 7, Article ID 4020075, 2020.

[30] A. M. Talmon and A. Bezuijen, "Analytical model for the beam action of a tunnel lining during construction," *International Journal for Numerical and Analytical Methods in Geomechanics*, vol. 37, no. 2, pp. 181–200, 2013.

[31] C. Zhao, A. Alimardani Lavasan, T. Barciaga, C. Kämper, P. Mark, and T. Schanz, "Prediction of tunnel lining forces and deformations using analytical and numerical solutions," *Tunnelling and Underground Space Technology*, vol. 64, pp. 164–176, 2017.

[32] K.-H. Park, K. Tantayopin, B. Tontavanich, and A. Owatsiriwong, "Analytical solution for seismic-induced ovaling of circular tunnel lining under no-slip interface conditions: a revisit," *Tunnelling and Underground Space Technology*, vol. 24, no. 2, pp. 231–235, 2009.

[33] A. Bobet, "Lined circular tunnels in elastic transversely anisotropic rock at depth," *Rock Mechanics and Rock Engineering*, vol. 44, no. 2, pp. 149–167, 2011.

[34] A. R. Kargar, R. Rahmannejad, and M. A. Hajabasi, "A semi-analytical elastic solution for stress field of lined non-circular tunnels at great depth using complex variable method," *International Journal of Solids and Structures*, vol. 51, no. 6, pp. 1475–1482, 2014.

[35] S. Wang, A. Lu, J. Tao et al., "Analytical solution for an arbitrary-shaped tunnel with full-slip contact lining in anisotropic rock mass," *International Journal of Rock Mechanics and Mining Sciences*, vol. 128, Article ID 104276, 2020.

[36] W. Ding, X. Wang, H. Zhu et al., "Defining method for designing load of multi-arch tunnel," *China Journal of Highway and Transport*, vol. 20, no. 5, pp. 78–82, 2007.
[37] H. Li and X. Guo, "Research on calculation methods of earth pressure on multi-arch tunnel for highway," *Rock and Soil Mechanics*, vol. 30, no. 11, pp. 3429–3434, 2009.
[38] Industrial Standard of the People's Republic of China, *Code For Design of Road Tunnel: JTG D70-2004*, Communications Press, Beijing, China, 2004.
[39] C. O. Aksoy, "Review of rock mass rating classification: historical developments, applications, and restrictions," *Journal of Mining Science*, vol. 44, no. 1, pp. 51–63, 2008.
[40] D. Li, X. Li, C. C. Li, B. Huang, F. Gong, and W. Zhang, "Case studies of groundwater flow into tunnels and an innovative water-gathering system for water drainage," *Tunnelling and Underground Space Technology*, vol. 24, no. 3, pp. 260–268, 2009.